Ann. Rev. Nucl. Part. Sci. 1988. 38: 217–77

LOW-NOISE TECHNIQUES IN DETECTORS

Veljko Radeka

Brookhaven National Laboratory, Upton, New York 11973

CONTENTS

1. INTRODUCTION

The question of "noise" arises in measurements on nuclear particles when we are interested in obtaining as precisely as possible the information about the energy, momentum, time of occurrence, or position of incidence of the particle on the detector. Most detection methods use ionization in a detection medium arising from the particle interaction. In some cases detection is a multistep process. For example, in transition radiation detectors, photons of a few keV produced by a relativistic particle in the radiator transfer their energy to one or more electrons in the inner shells of the atoms of gas in the detector, which in turn lose their energy by further

0163-8998/88/1201-0217$02.00

ionization of the gas atoms and molecules. In Čerenkov radiation detectors, each photon of a few eV, produced by a relativistic particle, is converted (under favorable circumstances) into a single electron by photoemission or ionization. Even when dealing with the light from scintillators, we convert the light signal into an electrical signal, since the electronic methods for processing small signals are much further developed than the optical methods. Thus, in all of these cases a measure of the information about the particle appears in the form of electric charge.

The precision of the measurement has several ramifications. To what extent does the measurement affect the particle, or what is the limitation on the accuracy of the measurement as required by the laws of quantum mechanics? What is the best detector that maximizes the charge as a measure of some quantity characterizing the detected particle? What is the best measurement of the charge produced in the detection process? This review is devoted to this last question, observation and measurement of the charge signal in particle detectors.

The charge in detectors is induced in the simplest case on a set of two electrodes for which ultimately only one parameter is important and that is their capacitance. Only a fraction of this charge is available for the measurement—one half in the optimal case. This fraction of charge is transferred to an amplifying device. The most appropriate devices for charge amplification are so-called charge-controlled devices, in which the current through the device (and through an output circuit) is controlled by the amount of charge in the conducting channel of the device. Such devices are all familiar amplifying devices, the vacuum tube, the bipolar transistor, and field-effect transistors of various types (junction gate, insulated gate, metal-semiconductor). Inherent to the conduction of current in these devices is a random component, either due to the generation of the current or to the thermal noise in the conducting channel, depending on the principle and the mode of operation, of the device. This random component associated with the amplification is the only noise that cannot be avoided in the charge measurement. The charge sensitivity of these devices, which is a measure of the gain, is inversely proportional to the carrier transit time through the channel,

$$dI_{out}/dQ_{in} = 1/t_c. \qquad 1.$$

While the input charge represents an increment that changes the state of the device and the output current, the charge in the output circuit increases with time so that the "charge gain" is proportional to the time duration t_m of the measurement,

$$Q_{out}/Q_s = (1/2)t_m/t_c, \qquad 2.$$

where Q_s is the charge induced on the detector electrodes. (One half of Q_s appears on the amplifying device in the optimal case.) The amplifying device is followed by a filter, which in effect determines the averaging time for the noise or, in more exact terms, maximizes the signal-to-noise ratio for measurement of a desired quantity (amplitude as a measure of the energy loss of the particle, or time of the particle incidence on the detector, or in some cases the waveform of the induced charge versus time). In an optimized measurement, the lower limit for the charge uncertainty due to the noise in the amplifier (with a field-effect device) in terms of basic parameters is given by

$$\sigma_q = \mathrm{ENC}_{s\ \mathrm{opt}} \approx 4(2/3)^{1/2}(kTC_D)^{1/2}(t_c/t_m)^{1/2}, \qquad 3.$$

where k is the Boltzmann constant, T = temperature, C_D = detector electrode capacitance, t_c = carrier transit time through the amplifying device, and t_m = the measurement time. ENC is standard deviation in the charge measurement, commonly called the "equivalent noise charge."

This relation emphasizes three simple general criteria for low-noise charge measurements. First, and also important for other reasons, is a low detector capacitance. Second is a fast amplifying device with a short carrier transit time t_c. Third is a long measurement time t_m as allowed by the counting rate. Implicit in this relation is the condition that the amplifying device capacitance and the detector capacitance should be nearly matched.

In terms of these parameters, detectors used in different areas of physics research cover a very wide range. Charge-coupled devices (CCDs) are used for detection of x rays in astrophysics and for detection of minimum ionizing particles in particle physics (1). The capacitance of the sensing electrode is $C_D \approx 0.1$ pF, and an equivalent noise charge ENC ≈ 6 rms electrons has been obtained with a measurement time $t_m \approx 10$ μs. This corresponds to an energy resolution for x rays of ~ 50 eV (FWHM). At the other end of the scale are large ionization chamber calorimeters with liquid argon (2, 3). The electrode capacitance of these devices is of the order of 1 to 2 $\mu F/m^3$, the equivalent noise charge is of the order of 5×10^5 rms $e/(\mu F)^{1/2}$ for short measurement times of about 100 ns. The corresponding energy resolution is in the range of 2 $GeV/(m^3)^{1/2}$, which is sufficiently low for total energy measurements in the range of 100 GeV or more. An overview of various detectors in terms of these parameters is given in Figure 13 (Section 4.3).

Studies of noise in charge amplification had started concurrently with the use of gas ionization chambers and proportional detectors. The state of the art prior to semiconductor detectors is described in (4, 5). The advent of silicon and germanium detectors in the 1960s and the development of junction field-effect transistors (JFETs) provided an impetus to the

development and understanding of low-noise techniques for charge measurements (6–13). In connection with this work, methods for analyzing noise in the time domain were developed (14–17). This was particularly useful for understanding time-variant (switched parameter) signal-processing circuits. In this class of circuits signals and noise are filtered, for example, by multiple sampling and gated integration.

The developments of germanium detectors for γ-ray spectrometry in the range 10^{-2} to 10 MeV, of silicon detectors for charged particle experiments in the range 10^{-1} to 100 MeV, and of silicon detectors for x-ray spectrometry in the range 0.3 to 100 keV have reached maturity. Signal processing for these detectors is now well understood and highly developed (e.g. 10, 16, 18–23).

In the mid-1970s, experiments in high-energy physics started to make use of low-noise techniques, benefiting considerably from the state of the art developed for low-energy nuclear physics. The detectors particularly dependent on optimization of signals and noise were total absorption devices (calorimeters), particle-tracking detectors based on gas drift chambers and on position sensing by charge division, and transition radiation detectors.

The measurement of the position of particle incidence on the detector plane has been of great interest in several quite different areas of research. High-resolution position sensing is usually based on interpolation. Interpolation methods are based either on the division of induced charge according to the position, or on time interpolation, where the particle position is converted into time by charge drift to the sensing electrode or by injection of the induced charge into a delay line. In all of these methods the interpolation factor and the position resolution are limited by the signal-to-noise ratio. Various position interpolation methods have been developed and their resolution limits studied (24–27). Detectors largely different in design and size have evolved in different areas of research. Large time projection chambers are used for particle tracking in high-energy physics (28). Signal-processing questions with gas and liquid time projection chambers are discussed in (29, 30). Position-sensitive detectors are used in crystallography and for molecular structure determination by x-ray and neutron scattering. Position resolution limits and low-noise techniques for some of these detectors are explored in (31–34).

Recent increased interest in vertex detectors in high-energy particle physics has stimulated the development of silicon detectors with a position resolution in the range of a few micrometers. The three detector concepts for particle position sensing that are currently receiving the most attention are microstrip devices (35), charge-coupled devices (1), and silicon drift chambers (36). These detectors are very thin (typically less than 300 μm),

and the signals produced by minimum ionizing particles are quite small (from 10^3 to 10^5 e). Some signal-processing questions are analyzed in (37–39). In small detector elements ("pixels") with a capacitance of less than about 1 pF, the lowest noise is achieved if the charge amplifier is on the same substrate as the detector. This has been realized only on CCDs so far. For larger pixels it is sufficient for the amplifier to be on a separate silicon chip close to the detector. A number of monolithic readout circuits for "microstrip" or "pixel" detectors have been or are being developed (40–43). Realization of an amplifier on the same substrate as the detector on high-resistivity silicon presents some unique problems (44). An amplifier on high-resistivity silicon for integration with a silicon drift chamber is being developed (45).

The development of monolithic low-noise readout circuits is essential for very large and complex detectors for future experiments in particle physics, and also for x-ray detectors for very high counting rates for use at synchrotron radiation facilities. Only with such monolithic circuits will it be possible to build detectors for the high particle multiplicities arising at high particle energies and with relativistic heavy ions.

Monolithic circuits make possible new signal-processing methods since certain functions, such as multiple sampling and switching of capacitors, can be easily realized. The noise of monolithic devices is, in most cases, higher than for a discrete device with equal parameters, and a low noise in charge measurements is achieved by low-capacitance electrodes and amplifiers where that is possible. Clearly, further study of time-variant signal processing and of the noise sources in monolithic devices is necessary.

We concentrate in this review on the fundamentals of low-noise techniques and on understanding the limits in charge signal measurements. A detailed description of numerous techniques is not feasible within the limitations of space here. The fundamental limits are essential as a reference in determining the degradation in the measurement accuracy caused by the compromises that must be made in the very large and very complex detectors of interest today and in the future. The best results are usually achieved when the simple picture outlined earlier in this introduction can be approached, where only the amplifier inherent noise is present and the detector and amplifier capacitances are nearly matched and as low as possible.

2. CHARGE COLLECTION AND SIGNAL FORMATION IN DETECTORS

The signal observed on the electrodes of a detector is induced by the motion of charge carriers in the space around the electrodes. The term

charge carrier applies in this case to positively and negatively charged ions (e.g. electrons and positive ions in a gaseous or liquid medium, electrons and holes in a semiconductor) produced by the interaction of the nuclear charged particle with the detection medium via one or more processes such as ionization, excitation, emission, and avalanche multiplication. In most cases the velocity of the moving carriers is low compared to the velocity of light, so that the magnetic field effects of the moving carriers can be neglected. The induced current and charge can be calculated then based only on the laws of electrostatics. Methods for calculation have been developed, and special cases of various detectors have been analyzed (37, 46–50).

2.1 *Current Induced by a Moving Charge and the Weighting-Field Concept*

Calculations of the induced current (charge) are based on the reciprocity theorem, also known as Green's theorem (50) or as Gauss identity. This theorem defines the relation of potentials and charges on a multielectrode system for the two states before and after one or more potentials and charges are changed. In the general case, the electrodes are allowed to "float," i.e. to be connected to arbitrarily high impedances. In most situations with multielectrode detectors, all the electrodes are connected either to amplifiers with a low input impedance or to sources of dc potentials (bias) with a low impedance for signal frequencies of interest (in practice, with capacitors to ground larger than the interelectrode capacitances). Thus the motion of charge carriers does not affect the electrode potentials. This simplifies the expression for the induced charge. The reciprocity theorem for many electrodes is usually given in the form,

$$\sum_i Q_i V_i' = \sum_i Q_i' V_i, \qquad 4.$$

where Q_i, V_i are initial values, and Q_i', V_i' are the values after the change of state. We get a better intuitive grasp if we consider only two electrodes, where the potential of only one electrode is changed in each state by V_1 and V_2', respectively. Then we have,

$$Q_1' V_1 = Q_2 V_2'. \qquad 5.$$

An externally applied potential V_1 on electrode 1 induces a charge Q_2 on electrode 2, and in the second state V_2' induces Q_1'. The ratio,

$$Q_1'/V_2' = Q_2/V_1 = C_{12}, \qquad 6.$$

defines the partial capacitance between these two electrodes, while all other electrodes are grounded (i.e. at constant potentials). The reciprocity in this

case describes the simple fact that the partial capacitance between any two electrodes is independent of the direction in which it is measured, or that electrostatic coupling is independent of the direction of charge displacement.

We now consider a charge in an interelectrode space as in Figure 1. If we assume that the charge q_m is on an infinitesimal electrode, and that electrode 1 is our sensing electrode, then by reciprocity,

$$q_m \cdot V_m = Q_1 V_1, \qquad 7.$$

(where q_m is caused by V_1 and Q_1 by V_m). We now determine the induced current $i_1 = dQ_1/dt$ due to the motion of charge q_m along a line segment $d\ell$ with a velocity $\mathbf{v} = d\ell/dt$,

$$i_1 = d(q_m V_m/V_1)/dt = q_m \frac{d(V_m/V_1)}{d\ell} \cdot \frac{d\ell}{dt}.$$

As the charge q_m (on the imagined infinitesimal electrode) moves away from electrode 1, the partial capacitance is decreased corresponding to a decrease in the ratio V_m/V_1 (since q_m is constant). V_m/V_1 represents a normalized potential at point m, and we can replace the differential term $d(V_m/V_1)/d\ell$ by

$$\text{grad}(V_m/V_1) = -\mathbf{E}_w. \qquad 8.$$

The normalized potential $V_m/V_1 = V_w$ and the normalized field $\mathbf{E}_w$ can be determined by applying a unity potential to electrode 1 and zero potential to all other electrodes. The induced current into electrode 1 is then

$$i_1 = -q_m \cdot \mathbf{E}_w \mathbf{v}. \qquad 9.$$

$\mathbf{E}_w$ is the weighting field in units of cm^{-1}, and it is a measure of electrostatic coupling between the moving charge and the sensing electrode. An example of the weighting-field shape is illustrated by the plot of equipotential lines in Figure 1*b* for planar geometry with strip electrodes. The weighting-field map is in general quite different from that of the operating field of the detector; the maps are identical only in some special cases.

We note that Equation 9 gives the induced current as a function of the position of the moving charge q_m. The procedure to calculate the current as a function of time (i.e. the waveform) is as follows. First, one finds the weighting field by solving Poisson's equation analytically or numerically for unity potential on the sensing electrode of interest and zero potential on all other electrodes. Next, the velocity of the moving charge as a function of position is determined from the operating (applied) field on the detector. This gives the induced current as a function of the position

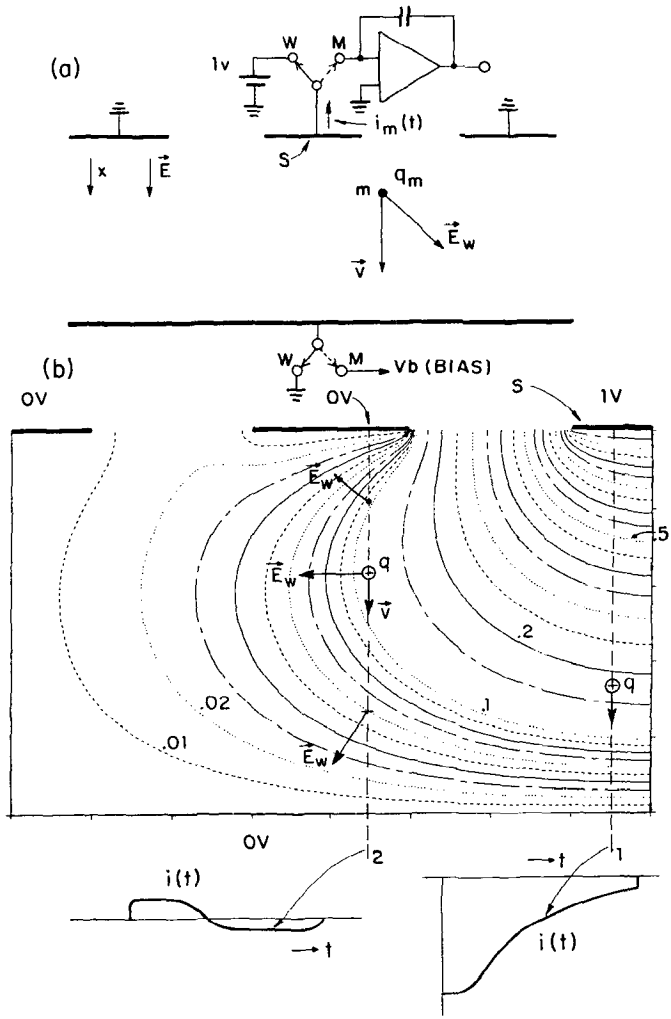

Figure 1 (*a*) Determination of the induced current by the weighting-field concept, illustrated on a planar multielectrode strip configuration. The weighting field is defined conceptually as the field for unity potential on the sensing electrode S (switch in position W) and zero potential on all other electrodes. In actual operation, the sensing electrode is connected to a charge amplifier and a uniform operating field is applied to the detector by connecting the opposite electrode to a voltage source V_b (switch in position M). The weighting field calculated numerically for this case is shown as a plot of equipotential lines in (*b*) for the left half of the electrode structure in (*a*). Two examples of charge transit from top to bottom are shown. The induced current waveforms, resulting from Equation 9 for a localized charge cluster moving at constant velocity, are shown at the bottom of the figure. Note the change in scale of equipotential lines from 0.01/step to 0.05/step.

of the moving charge. Third, the equations of motion are solved (which is necessary in the previous step in the case of ballistic motion of charge), and the resulting $x(t)$, $y(t)$, $z(t)$ are substituted in Equation 9 for $i_1(x, y, z)$ to obtain $i_1(t)$. (The minus sign results from the arbitrary assumption of induced current into the electrode being positive.)

If we are interested only in the total induced charge and not in the waveforms, we obtain from Equation 9, with $\mathbf{v} = \mathrm{d}\boldsymbol{\ell}/\mathrm{d}t$

$$Q_1 = \int i_1 \, \mathrm{d}t = -q_\mathrm{m} \int_{m_1}^{m_2} \mathbf{E}_\mathrm{w} \, \mathrm{d}\boldsymbol{\ell} = q_\mathrm{m}[V_\mathrm{w}(m_1) - V_\mathrm{w}(m_2)]. \qquad 10.$$

The induced charge is simply given by the difference in the weighting potentials between any two positions of the moving charge.

A great variety of results for the induced current and charge may arise in an electrode structure, such as in Figure 1, depending on the particle type detected (distribution of ionization) and on the ratio of the charge observation time (measurement time) and the charge carrier transit time. A simple example is given in Figure 1*b*. The current waveforms are drawn qualitatively. The operating field for this electrode configuration (e.g. semiconductor microstrip detector, liquid argon ionization chamber, etc) is usually uniform and perpendicular to the electrode planes. Charge q_m traversing the full distance between the electrodes along line 1 is observed as $Q_1 = -q_\mathrm{m}$, while the current decreases with distance from electrode 1, as the electrostatic coupling decreases. For a charge moving along line 2, the induced charge is zero if the measurement time is longer than the transit time. For a short measurement time a net induced charge is observed (the induced current waveform is bipolar, since the weighting-field direction changes along the path).

Some waveforms for semiconductor detectors are given in (37) and for liquid argon chambers in (2). Expressions for induced signals in a general case of many floating electrodes are derived in (49).

2.2 *Induced Current and Charge in Cylindrical Electrode Geometry*

We illustrate the application of the weighting-field concept to cylindrical electrode geometry since it applies to gas proportional and drift chambers. We use the calculated signal waveforms in the discussion of signal processing for these detectors in Section 6. These are obtained readily from Equation 9 for the current induced by a moving charge. A cylindrical gas proportional detector is illustrated in Figure 2*a*. We consider here the response to a single electron or to a localized cloud of electrons (such as produced by detection of a photon in the few keV range). As the electrons

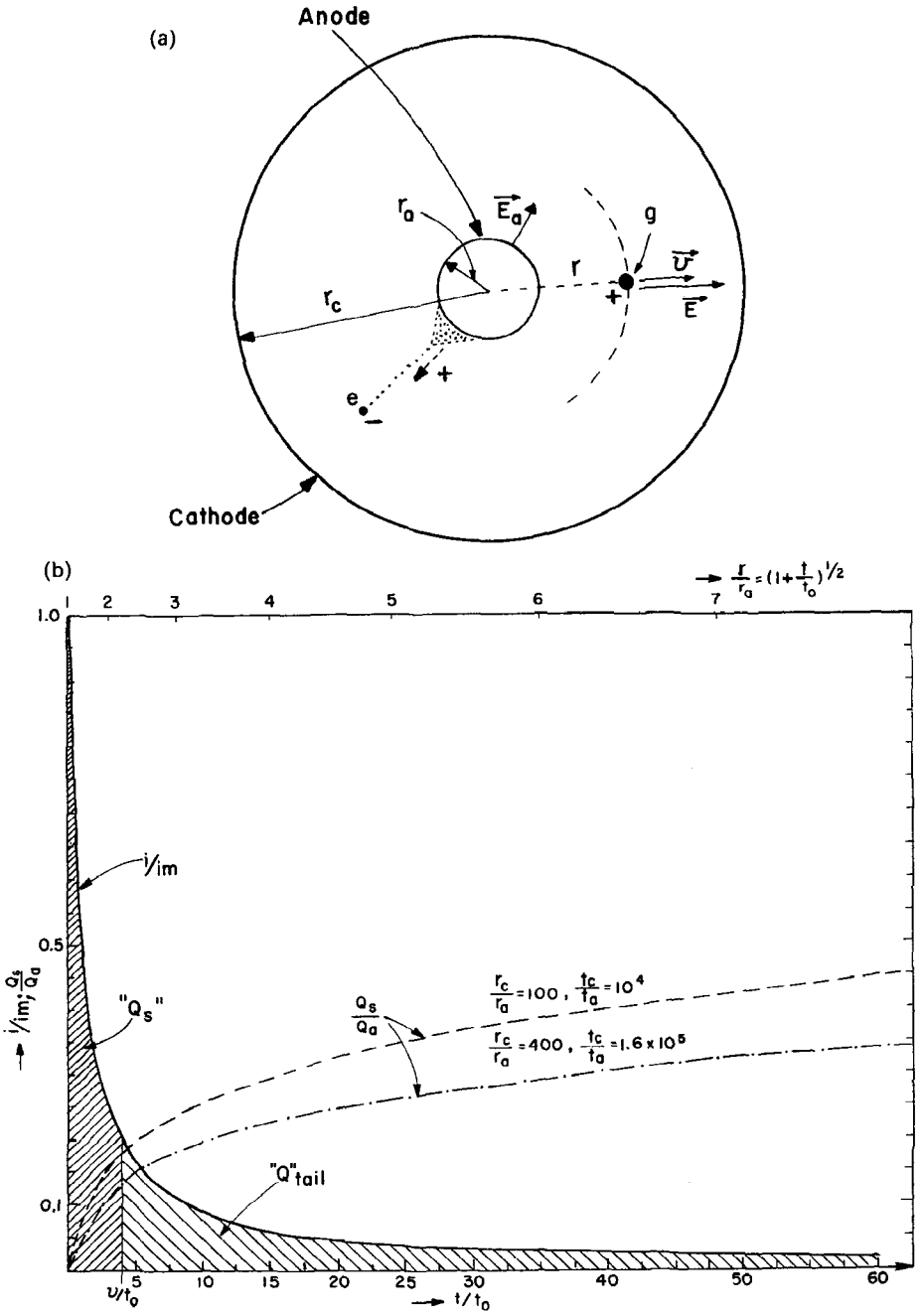

approach the high field region, an avalanche is created very near the anode wire. We now consider the signal induced by the motion of positive ions from the anode to the cathode.

The real electric field necessary for operation of the detector is produced by applying a voltage V between the anode and the cathode,

$$E = V[\ln(r_c/r_a)]^{-1} r^{-1} = E_a(r_a/r), \qquad 11.$$

where r_c = cathode radius, r_a = anode radius, and E_a is the operating electric field at the surface of the anode. By definition of the weighting field $\mathbf{E}_w$, it is obtained by applying unity potential on the sensing electrode (with respect to the cathode in this case). With $V = 1$ in Equation 11, we find

$$\mathbf{E}_w = [r \ln(r_c/r_a)]^{-1}. \qquad 12.$$

The operating field and the weighting field have the same direction and functional dependence in this case. The drift velocity of positive ions is then determined by the operating field and the mobility μ_+ of positive ions in gas,

$$\mathbf{v} = dr/dt = \mu_+ E_a r_a/r. \qquad 13.$$

The two vectors $\mathbf{E}_w$ and $\mathbf{v}$ have the same direction so that the scalar product in Equation 9 for the induced current as a function of the position of the moving charge becomes,

$$i(r) = -q\,\mathbf{E}_w\mathbf{v} = -q\,\mu_+ E_a r_a [r^2 \ln(r_c/r_a)]^{-1}. \qquad 14.$$

We now solve the equation of motion (Equation 13) for the radial distance versus time,

$$r^2 = r_a^2 + 2\mu_+ E_a r_a t = r_a^2(1 + t/t_0),$$

$$t_0 = r_a/(2\mu_+ E_a). \qquad 15.$$

The parameter t_0 determines the time scale of the ion motion and of the induced signal. The induced current and the charge as functions of time are

Figure 2 (*a*) Induced current and charge vs position of the moving charge and time for cylindrical electrode geometry. (*b*) Idealized single-electron response of gas proportional and drift detectors calculated from Equation 9, with a notation as in (*a*). The early part of the signal Q_s, typically only about 1/5 of the avalanche charge, is used in drift chamber timing and at high counting rates. The remaining tail (Q_{tail}) has to be cancelled by signal-processing circuits. Note that the signal of interest is produced while the positive ions have moved by only a few anode radii toward the cathode. The ratio r_c/r_a in (*a*) is shown smaller for clarity than in actual detectors, where $r_c/r_a \geq 100$.

$$i(t)/i_m = (1+t/t_0)^{-1}, \qquad \text{for } 0 < t/t_0 < (r_c/r_a)^2 - 1,$$

$$q(t)/q = [2\ln(r_c/r_a)]^{-1}\ln(1+t/t_0),$$

$$i_m = q[2t_0\ln(r_c/r_a)]^{-1}. \qquad 16.$$

The current and the charge as functions of the ion position are

$$i(r)/i_m = (r_a/r)^2$$

$$q(r)/q = \ln(r/r_a)/\ln(r_c/r_a). \qquad 17.$$

These relations describe the case in which the ions move from the surface of the anode ($r = r_a$) to the surface of the cathode ($r = r_c$). In a gas proportional detector, the last two steps of the avalanche multiplication take place very near the anode wire (within a few μm). Electrons produced in the avalanche move to the anode and because this distance is short contribute only a few percent to the induced signal. (The total induced charge due to the electrons and ions is, of course, equal to that produced by one carrier moving from one electrode to the other.) In most applications we can consider the induced signals as if the positive ions move from the anode to the cathode. The induced current and charge as functions of position and time are illustrated in Figure 2*b*. The values of the characteristic time parameter t_0 are about 1.5 ns for argon mixtures at 1 atm and typical detector parameters.

These curves represent an idealized "single-electron" response of gas proportional detectors. The discrepancies from these curves arise at very short times ($t/t_0 < 1$) from an electron component and from the possible dependence of ion mobility on the electron field at very high fields near the anode. The waveforms also differ at long times ($t/t_0 \gg 100$) in multiwire detectors where the cathode is not cylindrical. At high counting rates, one observes only the early part of the signal ($t/t_0 \leq 5$) and the rest is cancelled by pulse shaping. In this short time, only a small fraction of the charge produced in the avalanche is observed ($Q_s/Q_a < 1/5$). The signal shown in Figure 2*b* is produced by the motion of many positive ions. The diffusion of positive ions is quite small, so that the fluctuations in the signal shape are negligible for pulse-shaping purposes. For extended ionization tracks in the detector, the waveform becomes a superposition of many single-electron responses. The principles of operation of gas proportional detectors are described in (51) and the induced signals in multiwire chambers are analyzed in (52–54).

We note the distinction between the two cases illustrated in Figures 1 and 2. The operating and weighting fields have different forms in the multielectrode planar geometry with strip electrodes, and they have the same form for a simple two-electrode cylindrical geometry. We emphasize

the difference in the role of the weighting field and the operating field. The weighting field is determined only by the electrode configuration. The operating field is determined by the electrode configuration and by applied potentials on the electrodes. The charge motion is determined by the operating field and the properties of the medium (drift or ballistic motion). The induced signal waveforms are determined only by the weighting field and the motion of the charge carriers.

3. NOISE: ORIGIN AND PROPERTIES

We consider in this review the noise added in the measurement of induced charge, sometimes referred to as the "electronic noise," as distinguished from the "signal noise" due to the statistics of particle energy loss, ionization, and charge multiplication. Such noise may originate in the detector and in the circuit components and, as pointed out in the introduction, it is inherent to the amplification. We are interested in understanding the sources of the noise and in quantitative evaluation of its effect. We do not consider here "man-made" noise that originates in various electrical devices outside of our measurement apparatus. Of course, any such interference noise has to be eliminated before approaching the limits of measurement accuracy due to the electronic noise in the detector and the charge amplifier. In this section we briefly introduce some general properties of noise before discussing the noise in charge amplification in Section 4.

3.1 *Noise Process and Noise Variance*

The basis of a noise process can be represented as a sequence of randomly generated elementary impulses that has a Poisson distribution in time. Such a random sequence arises, for example, in electronic emission from a thermionic cathode (or photocathode) or in any charge carrier generation in which charge carriers with thermal (Boltzmann) distribution of energies have to cross a potential barrier. Each carrier induces a charge q in the collector (or sensing) electrode. Individual impulses may or may not be separated in time depending on their width (determined by the transit time in a particular device) and rate of occurrence $\langle n \rangle$. Upon acting on a physical system with impulse response much longer than $\langle n \rangle^{-1}$, the characteristic noise waveforms (e.g. those we observe on an oscilloscope) are produced as a superposition of responses to individual impulses. This is illustrated in Figure 3. A simple impulse response of relaxation type (e.g. a capacitor and a resistor at the sensing electrode) is assumed,

$$h(t) = C^{-1} U(t) \exp(-t/\tau), \qquad 18.$$

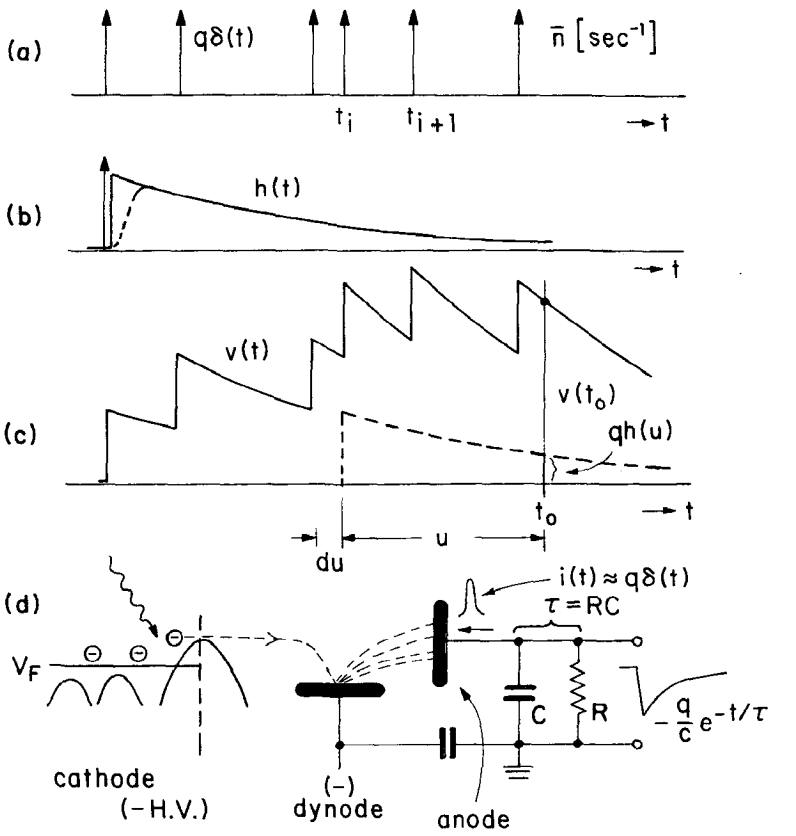

Figure 3 An illustration of a noise process. (*a*) Random sequence of elementary impulses generated by electron emission and multiplication (as in part *d*). (*b*) Impulse response of the output circuit. (*c*) Superposition of responses to individual impulses. Variance is calculated using Campbell's theorem (Equations 19, 20). (The external circuit for the induced current is closed through C and R in the output and the dynode bypass capacitance.)

where $U(t)$ is a unit step function. We are interested in the measurement error due to the noise at an observation time t_0, when a signal is observed (the signal is not shown in the figure). The amplitude of the noise at t_0 is the result of many randomly generated noise impulses.

A simple tool for calculation of the noise variance is Campbell's theorem (14, 15, 48, 55), which states that the sum of mean square contributions of all preceding impulses equals the variance. The contribution at time t_0 of an impulse occurring at time t_i is $v_i(t_0) = qh(t_0 - t_i) = qh(u)$. By using Campbell's theorem and subtracting the mean value, one obtains

$$\sigma^2 = \langle v^2(t_0)\rangle - \langle v(t_0)\rangle^2 = q^2 \sum_i h^2(t_0 - t_i). \qquad 19.$$

For a very high rate of impulses, $\langle n\rangle\tau \gg 1$, we can use continuous variables and write for a contribution to the variance at t_0 from impulses generated in the time interval du, $d\langle v^2(t_0)\rangle = q^2h^2(u)\langle n\rangle\, du$. We add all the previous history and obtain,

$$\sigma^2 = \langle n\rangle q^2 \int_{-\infty}^{\infty} h^2(u)\, du. \qquad 20.$$

We have made use of the assumption that the random process is stationary so that σ^2 is independent of the time t_0 of the measurement. Integration limits $(-\infty, \infty)$ signify that the integration has to be carried out for all nonzero values of the impulse response $h(u)$ independently of the origin of the time variable u.

We can see that the noise variance is determined by the noise process, the rate of impulses $\langle n\rangle$, and their area q (charge), and by the impulse response $h(t)$ of the measurement system. If we measure σ^2 and $h(t)$, we can determine $\langle n\rangle q^2$, but we cannot determine $\langle n\rangle$ and q from this measurement. Only when randomly generated carriers move in one direction, which results in a mean current $I_0 = \langle n\rangle q$, can the rate and the charge of impulses be determined from σ^2 and I_0. In such a case we may say that the current is associated with "shot noise." The integral of the system response squared is simply a measure of the width of the response and can be written as

$$\int h^2(t)\, dt = \tau_F a_{F2}, \qquad 21.$$

where τ_F defines the length of the impulse response and a_{F2} is its form factor. The variance in the charge measurement due to the shot noise is then,

$$\sigma^2 = I_0 q \tau_F a_{F2} = \langle n\rangle q^2 \tau_F a_{F2}. \qquad 22.$$

This result has been derived without any reference to noise description in the frequency domain in terms of the noise power spectrum and power spectral density. The impulse response $h(t)$ is a description of the measurement system in the time domain. Its Fourier transform $H(\omega)$, called the transfer function, describes the system response in the frequency domain. The total "energy" of the system response is independent of whether the output is analyzed in terms of time or frequency, so that we can write,

$$\int_{-\infty}^{\infty} h^2(t)\,dt = \frac{1}{2\pi}\int_{-\infty}^{\infty} |H(\omega)|^2\,d\omega.$$

This equality follows formally from Parseval's theorem (7, 48). Since $|H(\omega)|^2$ is an even function (and with $\omega = 2\pi f$),

$$\int_{-\infty}^{\infty} h^2(t)\,dt = 2\int_{0}^{\infty} |H(\omega)|^2\,df.$$

The noise variance is then,

$$\sigma^2 = 2\langle n\rangle q^2 \int_0^{\infty} |H(\omega)|^2\,df. \qquad 23.$$

This relation represents an integrated power spectrum at the output of the system. Since the output power spectrum $W_{out}(\omega) = W_{in}(\omega)|H(\omega)|^2$, the input power spectral density is clearly

$$W_{in}(\omega) = 2\langle n\rangle q^2 = W_0. \qquad 24.$$

The power spectrum for the shot noise is uniform (i.e. white), as is well known for a random sequence of impulses (e.g. Figure 3*a*). The high frequency cutoff of the process is inversely proportional to the width of the elementary impulse, which is determined by the details of the noise impulse signal formation (e.g. electron transit time from the dynode to the anode in Figure 3*d*). The term "power" in the discussion of power spectra refers to the amplitude squared of any variable observed (e.g. current, voltage, or charge). Thus we can use power spectral density for white noise in calculations of the noise variance from the system time response,

$$\sigma^2 = \frac{1}{2} W_0 \int_{-\infty}^{\infty} h^2(t)\,dt. \qquad 25.$$

THERMAL NOISE The noise in resistors arises from the thermal motion of charge carriers. When the resistor is in thermal equilibrium with its surrounding, the mean value of potential difference between the ends of the resistor is zero. However, Brownian motion of the charge carriers results in a fluctuating potential difference (i.e. electromotive force—emf) across the resistor. The thermal noise in resistors has been studied by Nyquist (56) and Johnson (57). The resistor can be represented as a generator of noise, either as a current source in parallel with the resistance R, or by Thevenin's equivalence, as a voltage source in series with R, where $v_n = i_n \cdot R$. The power spectral density based on statistical thermodynamics (56) is given here for the current source,

$$W_i(f) = 4hf\,[\exp(hf/kT) - 1]^{-1} R^{-1}, \qquad 26.$$

where h = Planck constant, k = Boltzmann constant. Except for very low temperatures, the high-frequency limit of the thermal noise process is well beyond the frequencies of interest in detector signal processing. In this case, $hf/kT \ll 1$ and the spectral density in the frequency range of interest becomes white,

$$W_{i0} = 4kT/R. \qquad 27.$$

We can use this expression to calculate the variance in the measurement of the charge signal by using Equation 25 in the same way as for the shot noise.

SHOT NOISE VS THERMAL NOISE—SIMILARITIES AND DIFFERENCES The shot noise represents fluctuations in the number of current carriers emitted from a cathode (as in Figure 3*d*), and there are no other current carriers present, except for those contributing to the net current flow in one direction. In a resistor, there are many free or activated carriers present in thermal random motion. The net current flow in one direction, caused by an applied electric field, results from a small displacement of carriers superposed to the thermal motion. Thus the thermal noise is independent of the dc current in the resistor. An exception to this is excess noise arising at higher current densities in certain resistor materials (e.g. carbon), where some different conduction mechanisms are involved. Thermal noise can also be thought of as a random sequence of elementary impulses (induced by thermal motion of carriers) where Equation 27 corresponds to Equation 24. As with the shot noise, the spectral density alone does not reveal any information about the rate $\langle n \rangle$ and the elementary impulse charge q. However, as shown by derivation of Equation 25, the power spectral density is sufficient to calculate the variance.

The formal equivalence between the effects of the shot noise and the thermal noise can be carried a little further to ask what value of resistance contributes equal noise to the shot noise of a current I_0. From Equations 22, 24, and 27, we obtain, with $q = e$,

$$RI_0 = 2kT/e \approx 50 \text{ mV} \qquad \text{at } T = 293 \text{ K}. \qquad 28.$$

The "50-mV rule" is useful for estimating the relative contributions of noise, for example from the base current of a transistor and a biasing resistor (if $RI_0 > 50$ mV, the shot noise of I_0 is dominant).

There are cases in which the observed current I_0 on an electrode is not a measure of the shot noise. In semiconductor devices, I_0 may be a result of two (or more) current-generating mechanisms, such that $I_0 = I_{01} - I_{02}$. Since the noise from these sources is uncorrelated, the total shot noise

density will be $W_0 = 2(I_{01}+I_{02})e$, and therefore it could be much larger than expected from the net current I_0.

3.2 *A Model for Generation of Noise Spectra*

We now consider how different noise spectra encountered in charge measurements may arise. Since the noise spectrum of a random sequence of impulses is white for frequencies of interest, the subsequent physical system upon which the noise acts determines the noise spectrum at the output of the system. The physical system may be as simple as a single capacitance (single integration), a more complicated one such as a diffusive process, or an entire measurement system. The original white spectrum W_0 is transformed into $W(\omega)$ by the system transfer function $H(\omega)$, so that $W(\omega) = |H(\omega)|^2 W_0$. The impulse response $h(t)$ of the system is the Fourier transform of the transfer function, and each elementary impulse is transformed into a pulse of the shape $h(t)$. This is illustrated in Figure 4 for three simple cases of most interest here. The first is a relaxation process, Figure 4*b*, as already shown in Figure 3. The impulse response is

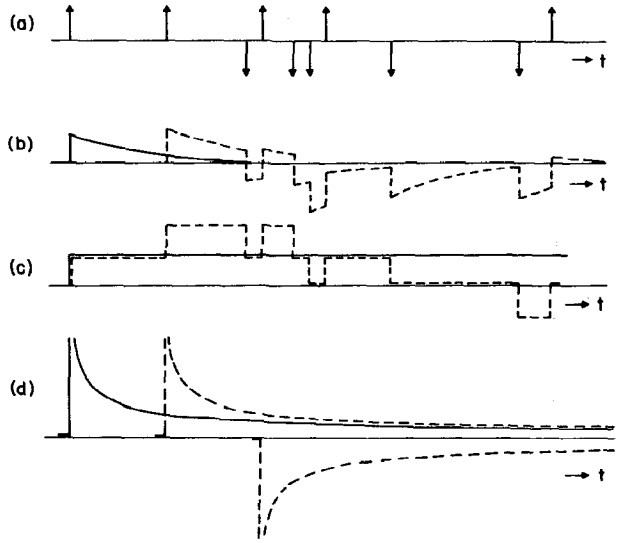

Figure 4 A model for generation of noise spectra. Superposition of responses $h(t)$ for various transforming filters is shown. (*a*) Random sequence of elementary impulses has a white spectrum. (*b*) The relation $h(t) = U(t)\exp(-t/\tau)$ results in a $(1+\omega^2\tau^2)^{-1}$ spectrum. (*c*) An ideal integrator $h(t) = U(t)$ results in a random walk $1/f^2$ spectrum. (*d*) $1/|f|$ noise is generated by a transforming function $h(t) = U(t)t^{-1/2}$, which corresponds to half-order integration of white noise (58).

$h(t) = U(t)\tau^{-1}\exp(-t/\tau)$, and the transfer function $H(\omega) = (1+j\omega\tau)^{-1}$, which results in a well-known noise spectrum,

$$W(\omega) = W_0(1+\omega^2\tau^2)^{-1}. \quad 29.$$

Such a spectrum has two regions, for low frequencies $\omega\tau \ll 1$, it is flat or white, and for high frequencies $\omega\tau \gg 1$, it is $W(\omega) \propto \omega^{-2}$. In terms of filters, a circuit with this response is known as a first-order, low-pass filter.

We consider next the power-law noises, which can be represented as

$$w_\alpha(f) = |f|^\alpha, \quad 30.$$

where $w_\alpha(f) = W_\alpha(f)/W_\alpha(1\text{ Hz})$ is the normalized spectral density, and $W_\alpha(1)$ is the spectral density at 1 Hz per $\text{Hz}^{\alpha+1}$. The transfer function of the filter that transforms white noise into power-law noise is

$$H(\omega) = (j\omega)^{\alpha/2}, \quad 31.$$

and the corresponding impulse response obtained by the Fourier transform of $H(\omega)$ is

$$h(t) = U(t)K(\alpha)t^{-(1+\alpha/2)}, \quad 32.$$

where $K(\alpha)$ is a function of α. Two cases are of particular interest here. One is for $\alpha = -2$, which gives a $1/f^2$ spectrum, and it is obtained by a single integration, that is $h(t) = U(t)$. It represents a random walk in which each elementary impulse produces a step in the output variable, Figure 4*c*. The other is for $\alpha = -1$, which results in $1/|f|$ noise. The necessary transforming functions for $1/|f|$ noise are $H(\omega) = (j\omega)^{-1/2}$ and $h(t) = U(t)K(\alpha)t^{-1/2}$. This impulse response is illustrated in Figure 4*d*. Comparing the three cases in Figure 4, we note that different noise spectra result from different functional dependence of the "memory" in the system response. In the relaxation process original perturbation decays exponentially. Random walk has infinite memory (at least on the time scale of interest). The $1/|f|$ noise is based on a very slowly decaying memory ($t^{-1/2}$).

This brief discussion indicates how different noise spectra may arise. It is also apparent that the knowledge about the noise spectrum alone at some point in the system does not reveal much about the physics of the noise process. This is particularly true with noises of the $1/|f|$ type, for which $\alpha \approx -1$. Among many different mechanisms, this type of noise spectrum arises in random excitation of a diffusive medium, and in the case of exponentially decaying perturbations with a decay time constant probability $P(\tau) \propto \tau^{-2}$. A more detailed introduction to power-law noises and to the questions of low-frequency and high-frequency convergence of these noises is given in (58).

We can see from this discussion that we can encounter different noise

spectra at different points of the measurement system (at the detector and at the preamplifier output, for example). A measurement of the noise spectrum components and an accurate description of all spectrum-transforming functions of the system may aid us in determining the physical origin of noise, as discussed in Section 4.3.

We have considered so far some of the time and frequency properties of noise without any need to mention the amplitude distribution. In the simple model presented, the output variable is a result of the superposition in a linear system of a large number of random variables. According to the central limit theorem, this results in a gaussian amplitude distribution. A discrepancy from a gaussian amplitude distribution in a system noise measurement, with a signal simulated by a pulse generator, would indicate the presence of noise impulses at a much lower rate than from elementary impulses of the shot noise and the thermal noise. This may arise, for example, as a result of breakdown phenomena in the detector and amplifier components.

4. NOISE AND AMPLIFICATION OF CHARGE

In this section we discuss the relation of the intrinsic noise to the gain in amplifying devices, the role of filtering or pulse shaping, and the limits of charge sensitivity with respect to noise.

4.1 *Gain Mechanisms and Intrinsic Noise*

The gain mechanism, the speed of response, and the noise in electronic amplifying devices for the purpose of charge amplification can best be understood with the charge control concept. This concept is common to all devices that can potentially be used for charge amplification (e.g. bipolar transistor, vacuum tube, and all field-effect devices). We discuss it first in general and then for each device type of interest.

We usually think of these devices as three terminal devices. There is a control electrode to which charge is applied that controls the current flow between the two electrodes at the ends of a conducting channel. The current control takes place over some portion of the length of the channel. The charge carriers (electrons in the following discussion) spend time t_{el} in transit through this region of the channel. The channel current I_c is then related to the channel charge Q_c in the control region by

$$I_c = Q_c/t_{el}. \qquad 33.$$

This relation simply states that a charge Q_c is swept out into the collector (drain) electrode each time period t_{el}. Any change in the current can be caused only by a change in Q_c, which has to be supplied by the control

electrode. A change in the potential across the gate-channel junction in field-effect devices (i.e. base-emitter junction in bipolar transistors) is associated with a change in the channel charge. A change in charge associated with a change in voltage leads to what might be defined as a control capacitance C_c,

$$C_c = dQ_c/dV_{GS}. \quad 34.$$

It is customary to define the ratio of the change in the output current and the change in the potential of the control electrode as a transconductance $g_m = dI_c/dV_{GS}$. The ratio of the current change and the change in the channel charge is a measure of the amplification,

$$dI_c/dQ_c = t_{el}^{-1} = g_m/C_c. \quad 35.$$

An increment in the input charge causes a change in the output current (with a response time $\sim t_{el}$). To obtain a charge gain, we have to wait for the charge at the output to accumulate so that the gain increases with the measurement time t_m,

$$dQ_{out}/dQ_c = t_m/t_{el}. \quad 36.$$

These relations illustrate the basic role of the electron transit time in the device. We consider now the quantities g_m/C_c, g_m, I_c, and t_{el} in terms of device parameters.

FIELD-EFFECT DEVICES The principles of operation of the junction field-effect transistor (JFET) and of the metal-oxide (MOSFET) transistor are illustrated in Figure 5.

The conducting channel depth in a JFET is controlled by the depletion region from the highly doped gate electrode into the channel. The depletion region profile is strongly influenced by the potential drop along the channel caused by the flow of the current from the drain electrode to the source. As the drain potential is increased, a point is reached where the channel is pinched off, and from there on the drain current increases little with the drain potential. The device is operated in this region as an amplifier, and the current control by the gate potential takes place in the region between the pinch-off point and the source by the variation in the depletion region and the remaining channel.

In a MOSFET the basic mechanism is similar, although the details are quite different. In a so-called enhancement-type device, the channel is created by inversion of the layer (p-type in this case) under the gate oxide. In this layer a sheet of electrons is induced under the gate oxide, which creates a conducting channel between the source (n^+) and drain (n^+). The gate-to-source voltage necessary to initiate the channel is called the

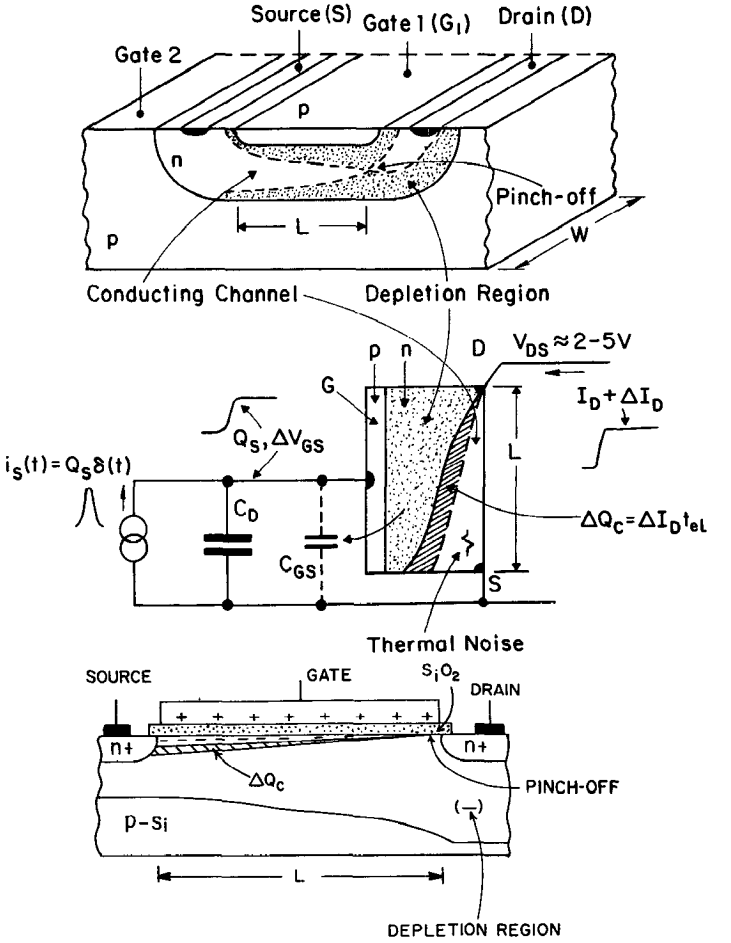

Figure 5 Charge control concept in field-effect transistors. (*Top*) Cross section of a typical n-channel junction field-effect transistor structure. (*Middle*) Detector capacitance and the current control section of the transistor. Shaded area represents a change ΔQ_c in the channel charge necessary to change the channel (drain) current by ΔI_d. The term t_{el} is the electron transit time through the channel L. (*Bottom*) Cross section of a typical n-channel MOS transistor. Density of electrons in the induced sheet (channel) under the oxide and the charge increment ΔQ_c are indicated graphically.

threshold voltage V_t. Both types of devices can be described by the same approximate relations. The drain (channel) current I_{DS}, the transconductance g_m, and the g_m/C_{GS} ratio in the pinch-off region are given by (8, 59–61)

$$I_{DS} \approx \frac{1}{2}\mu\frac{C_{GS}}{L^2}(V_{GS}-V_T)^2,$$

$$g_m \approx \mu\frac{C_{GS}}{L^2}(V_{GS}-V_T) = \left(2\mu\frac{C_{GS}}{L^2}\right)^{1/2} I_{DS}^{1/2},$$

$$\frac{g_m}{C_{GS}} \approx \frac{\mu}{L^2}(V_{GS}-V_T) = \frac{1}{t_{el}}, \qquad 37.$$

where μ is the electron mobility, C_{GS} = gate-source control capacitance, V_{GS} = gate-to-source voltage, V_t = threshold voltage, and L is the length of the controlled channel region indicated approximately in Figure 5.

These relations are in the form for a MOSFET in terms of V_{GS} and V_T. For a JFET, $V_{GS}-V_T$ can be written $V_p(1-V_{GS}/V_p)$, where V_p is the pinch-off potential and V_{GS} is the absolute value of the reverse gate-to-source voltage. The potential difference $(V_{GS}-V_T)$ for MOSFETs is in the range of 1–5 V, the pinch-off voltage for JFETs is 1 to 3 V, and V_{GS} is 0.5–2 V. We can now estimate the electron transit time. The channel length in MOSFETs used for amplifiers and analog circuits is $L = 3$ μm for the better understood fabrication processes. The channel length in JFETs for a well-established process for low-noise devices is $L \approx 7$ μm. The electron mobility in bulk silicon is $\mu_- \approx 1.3 \times 10^3$ cm^2 V^{-1} s^{-1}. This value can be used for estimation in JFETs. In MOSFETs the mobility of electrons at the silicon–silicon dioxide interface is lower (by a factor of 2 to 3). For a JFET with $V_p(1-V_{GS}/V_p) = 1.5$ V, this gives for the electron transit time $t_{el} \approx 0.25$ ns. We note that the average field along the channel is $E_c \approx (V_p-V_{GS})/L \approx 2.5 \times 10^3$ V/cm. The electron drift velocity in silicon saturates completely at $E \approx 10^4$ V/cm, so that even with this relatively long channel (7 μm), the device is close to velocity saturation effects. For short channels in the velocity saturation region, a lower limit for the electron transit time is simply

$$t_{el} \approx L/v_{sat}. \qquad 37a.$$

The carriers do not reach saturation velocity along the whole channel, so that the transit time is usually longer than given by this limit (59).

BIPOLAR TRANSISTORS The principle of charge control in a bipolar transistor is illustrated in Figure 6 on an idealized npn structure. Minority carriers (electrons) are injected from the emitter into the base. They diffuse across the base and are swept away by the field between the base and the positively biased collector. The diffusion current through the base is

$$I_c = eD_n\, dn_p(x)/dx, \qquad 38.$$

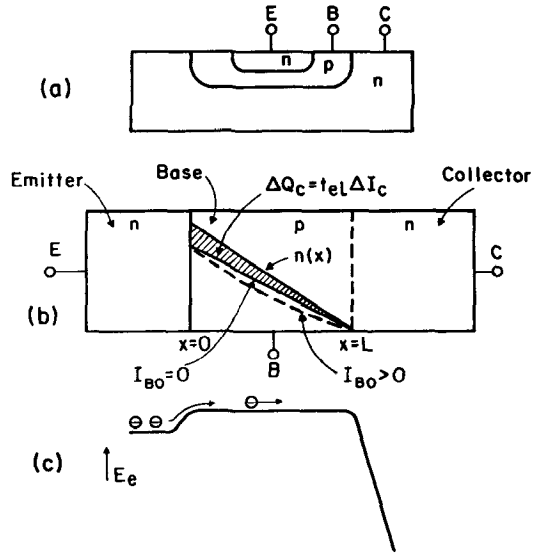

Figure 6 Charge control in a bipolar transistor. (*a*) Cross section of a typical npn planar bipolar transistor structure. (*b*) Idealized transistor structure with minority carrier concentration in the base illustrated. Shaded area represents a change in the base charge necessary to change the collector current by ΔI_c; t_{el} is the electron transit time through the base. (*c*) Relative potential energy for electrons injected into the base. The emitter-base junction is forward biased and the collector-base junction is reverse biased.

where D_n is the diffusion coefficient and $n_p(x)$ is the concentration of minority charge carriers (electrons) in the base. To maintain the charge equilibrium, the concentration of excess majority carriers (holes) has to be equal to that of diffusing electrons. If no minority carriers are lost in transit by recombination, the current by diffusion through the base is constant and a linearly decreasing charge concentration is established. The collector current is then

$$I_c = D_n e n_p(0)/L = 2D_n Q_c/L^2, \qquad 39.$$

where Q_c is the charge in the base. From this and from Equation 33, the electron transit time through the base is

$$t_{el} = L^2/2D_n. \qquad 40.$$

To change the collector current, a change in the base carrier concentration is necessary, as indicated in Figure 6, and this charge has to be supplied into the base-emitter circuit (by the signal). Charge injection requires a change in potential across the emitter-base junction. The current across the junction, from Boltzmann distribution of energies, is $I_c = I_{c0} \exp$

(eV_{BE}/kT), where I_{c0} is the thermally generated current, so that the transconductance is

$$g_m = dI_c/dV_{BE} = I_c e/kT. \quad 41.$$

The potential change dV_{BE} associated with the charge $dQ_c = dI_c t_{el}$ defines the diffusion capacitance, i.e. the current control capacitance (C_c in Equation 34) between the base and the emitter:

$$C_{dif} = t_{el} I_c e/kT = t_{el} g_m. \quad 42.$$

The base length L is of the order of a few tenths of a micrometer in high-speed transistors. By Einstein's relation (59), $D_n = \mu_c kT/e \approx 30$ cm^2 s^{-1}. A base thickness of 1 μm would result in a transit time $t_{el} \approx 0.16$ ns. An essential feature of modern transistors is that they have an internal drift field produced by a graded doping concentration across the base. This adds a drift component to the velocity of electrons diffusing across the base. Equation 40 is not valid for devices with a built-in drift field, but the basic relations in Equations 41 and 42 remain valid. Devices with t_{el} in the range of 30–50 ps are common, and faster devices are being developed (both as discrete and monolithic devices).

In bipolar transistors, some of the minority carriers recombine in transiting the base, and the majority carriers (holes) have to be supplied to maintain continuously the equilibrium. The resulting base current is determined by the minority carrier life time τ_r, $I_B/I_c \propto t_{el}/\tau_r$. The ratio $I_c/I_B = h_{FE}$ is known as the transistor dc current gain. This is a somewhat misleading term, since the dc base current is a measure of imperfections and not a part of the gain mechanism. In the absence of recombination, an increment of charge is required to establish a collector current and not a steady base current. The importance of the base current (on the negative side) is that it generates shot noise in the input circuit of the detector and amplifier.

NOISE IN AMPLIFYING DEVICES The current conduction in field-effect devices is by majority carriers, where the channel is in a sense a variable conductance. The intrinsic noise in field-effect transistors is the thermal noise of the conducting channel modified by the effect of channel width modulation. It can be represented as a thermal noise current added to the channel (drain) current I_{DS}, that is, as a current noise generator in parallel with the conducting channel. It can be expressed in terms of the transconductance, which is equal to the conductance of the channel at $V_{DS} = 0$ and $I_{DS} = 0$ (8). The drain current spectral density is (62)

$$\langle i_D^2 \rangle = 4kTa_n g_m. \quad 43.$$

The term a_n is weakly dependent on the gate bias. The theoretical value for typical operating conditions is $a_n \approx 2/3$; values $2/3 < a_n < 1$ have been found in practice.

In bipolar transistors the intrinsic noise appears as a shot noise in the collector current because carriers are randomly injected from the emitter into the base. As discussed in Section 3.1, Equations 22 and 24, the collector current spectral density is (with Equation 41)

$$\langle i_c^2 \rangle = 2eI_c = 2kTg_m. \qquad 44.$$

While this collector current injects noise into the output circuit, the base current injects shot noise into the input circuit, $\langle i_B^2 \rangle = 2eI_B$, where $I_B \ll I_c$.

The intrinsic noise of amplifying devices is described as the output current spectral density in terms of the transconductance g_m. It can also be represented as equivalent fluctuations in the potential of the input (control) electrode, as $\langle v_G^2 \rangle = \langle i_D^2 \rangle / g_m^2$. These potential fluctuations can be thought of as being produced by the thermal noise in an equivalent resistance R_s in series with the input electrode. Then we have

$$\langle v_G^2 \rangle = 4kTR_s$$

$$R_s = a_n/g_m, \qquad 45.$$

where $a_n \approx 2/3$ for field-effect devices and 1/2 for bipolar transistors. (For a historical comparison, $a_n \approx 2.5$ for the vacuum tube anode current shot noise.)

We can also express the intrinsic noise in terms of the charge induced on the detector electrode. If a charge q_s is induced on the detector electrode of a capacitance C_D, then the charge on the control electrode of the amplifying device will be $q_s C_c/C_D + C_c$). We can now define an equivalent input charge spectral density due to the amplifier intrinsic noise as $\langle q_{sn}^2 \rangle = \langle v_G^2 \rangle (C_D + C_c)^2$, and using Equations 37 or 42 and 45, write it in the following form,

$$\langle q_{sn}^2 \rangle = 4kTa_n(C_D + C_c)^2 g_m^{-1},$$

$$\langle q_{sn}^2 \rangle = 4kTa_n C_D \left[\left(\frac{C_D}{C_c} \right)^{1/2} + \left(\frac{C_c}{C_D} \right)^{1/2} \right]^2 t_{el}. \qquad 46.$$

We note that this is the charge spectral density and that the equivalent noise charge that we are interested in is calculated in Section 4.2. We can already see the importance of the electron transit time, t_{el}, and we discuss its implications in the next section. The noise expressions have been derived based on g_m and C_c and by the relation of this intrinsic parameter $C_c/g_m = t_{el}$. The parasitic capacitances and series resistances of the tran-

sistor electrodes make the measured values of the device input capacitance C_A higher, and the transconductance lower, so that the measured device time constant $\tau_A = C_A/g_m$ will always be larger than t_{el}. The value of t_{el} will still determine the frequency at which the transconductance decreases to $1/\sqrt{2}$ of its low-frequency value $f_T \approx (2\pi t_{el})^{-1}$.

4.2 *Equivalent Noise Charge Calculation*

We showed in Section 3.1 how the variance in the charge can be calculated for the noise current flowing into the detector sensing electrode (Equations 21, 22, 24, 25). The variance is determined simply by the noise current spectral density W_0, i.e. the "rate" $\langle n \rangle q^2$ of the noise process, and the system response $h(t)$. We normalize the system impulse response $h(t)$ so that a unit (charge) impulse of current $\delta(t)$ into the detector electrode produces an output response whose maximum value is unity. Then the standard deviation σ_q is simply an "equivalent noise charge" (ENC) equal to a signal $Q_s = \sigma_q$ that would produce the same output amplitude.

We can represent such a noise source as a current generator in parallel with the detector electrode capacitance, as illustrated in Figure 7. The equivalent noise charge for such parallel sources of noise is then,

$$\mathrm{ENC}_p = \frac{1}{2} W_0 \int_{-\infty}^{\infty} h^2(t)\, dt, \qquad 47.$$

where $W_0 = 2eI_0$ for the shot noise (e.g. from detector leakage currents, input transistor base current) and $W_0 = 4kT/R_p$ for the thermal noise from resistors connected to the detector sensing electrode.

To determine the ENC for the noise contribution by the amplifying device, we have to take into account that this noise acts differently upon the detector-amplifier circuit than a noise current into the input. As seen in the preceding section, the intrinsic transistor noise appears as fluctuations in the current through the conducting channel, and therefore in the output current. From the elementary model in Section 3.1, we can think of this noise as a random sequence of impulses in the (drain or collector) current of the amplifying device. An elementary impulse of the drain current corresponds to an elementary impulse of charge and voltage at the input electrode (gate), and the charge spectral density for this equivalent noise at the input is given by Equation 46.

We note in Figure 5 that a current impulse $i(t) = Q_s\delta(t)$ into the input electrode is integrated on the capacitance $C_D + C_{GS} = C_{in}$ and becomes a step of voltage $(Q_s/C_{in})U(t)$ at the gate, which results in a step $Q_s(g_m/C_{in})U(t)$ in the channel current. Conversely, an impulse in the channel current $q(g_m/C_{in})\delta(t)$ can be thought of as being caused by an impulse

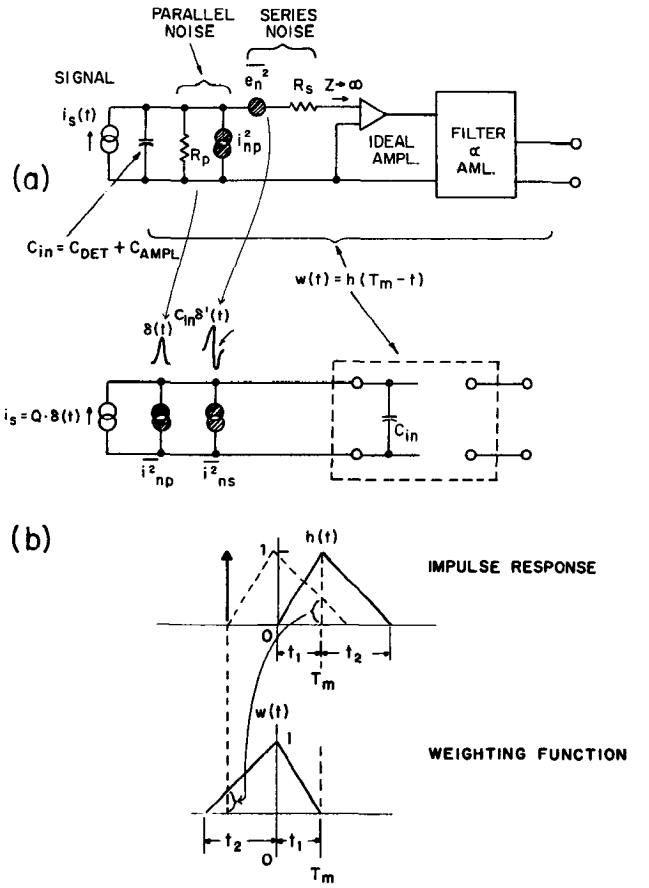

Figure 7 Equivalent circuit of detector and amplifier for noise analysis. (*a*) Location of white noise sources in the circuit. The series noise represents the noise in the conducting channel of the amplifying device. (*b*) Equivalent circuit with the series noise voltage source transformed into a current source by differentiation. The impulse response $h(t)$ is defined with respect to the signal current generator and it includes the detector-amplifier capacitance C_{in}. The weighting function $w(t)$ is a mirror image in time of the impulse response with respect to the time of amplitude measurement T_m.

$(q/C_{in})\delta(t) = v_0\delta(t)$ in the gate voltage, and in terms of the input current by a doublet $q\delta'(t)$, where $\delta'(t)$ is the derivative of the delta function $\delta(t)$.

We can now apply Campbell's theorem from Section 3.1 (Equations 20, 25). We can integrate the contributions to the system output of the random sequence of noise impulses in the voltage or charge at the input or, alternatively, of the doublets in the input current. The response of a system with an impulse response $h(t)$ to a doublet $\delta'(t)$ is the derivative $h'(t)$ of

the impulse response, since by convolution $\delta'(t) * h(t) = h'(t)$. Remembering the relation $\langle n \rangle q^2 = W_0/2 = \langle q_{sn}^2 \rangle/2$ between the "rate" and charge of elementary impulses and the noise spectral density, and applying Campbell's theorem to the intrinsic noise of the amplifying device, gives us an equivalent noise charge of

$$\mathrm{ENC}_s^2 = \frac{1}{2}\langle q_{sn}^2 \rangle \int_{-\infty}^{\infty} [h'(t)]^2 \, dt. \qquad 48.$$

We shall express this relation in several different forms to make the relation among the detector, amplifier, and pulse-shaping parameters intuitively more obvious. The term $\langle q_{sn} \rangle^2$ is given by Equation 46, but we first discuss the amplifier noise in terms of an equivalent noise voltage generator, Equation 45, in series between the detector and an ideal amplifier, as illustrated in Figure 7. The location of this equivalent source of noise in the equivalent circuit has led to the term "series noise." The equivalent noise charge for both the series and the parallel noise in terms of the equivalent series and parallel noise resistances R_s and R_p, with $q_{sn} = C_{in} v_n$, can be expressed as,

$$\mathrm{ENC}^2 = (1/2) 4kTR_s C_{in}^2 \left[\int_{-\infty}^{\infty} [h'(t)]^2 \, dt + \frac{1}{\tau_c^2} \int_{-\infty}^{\infty} h^2(t) \, dt \right],$$

$$\tau_c = C_{in}(R_s R_p)^{1/2}. \qquad 49.$$

The relative contributions of the two sources of noise are clearly dependent on the relation of the time constant τ_c and the system impulse response $h(t)$. The significance and the meaning of τ_c (known as the "noise corner time constant") will become clearer in subsequent discussion.

Equation 49 raises the question, what is the optimum shape of the impulse response $h(t)$ to minimize the equivalent noise charge? The optimum impulse response can be found by using the calculus of variations (14) or by noting that the two terms involving integrals of a function and its derivative may be satisfied by an exponential function. The solution is

$$h_{opt}(t) = \exp(-|t|/\tau_c),$$

$$\mathrm{ENC}_{opt}^2 = 2kTR_s C_{in}^2/\tau_c. \qquad 50.$$

This function is known as the "cusp" or as the "matched filter," and it is shown in Figure 8. The matched filter concept is discussed in some detail in (5–7). This function implies an infinite delay (in practice only several times τ_c) between the event (induced current impulse) and the measurement time when the peak of the response is recorded. The tails of this function have a small effect on the measured noise. For example, if the system is

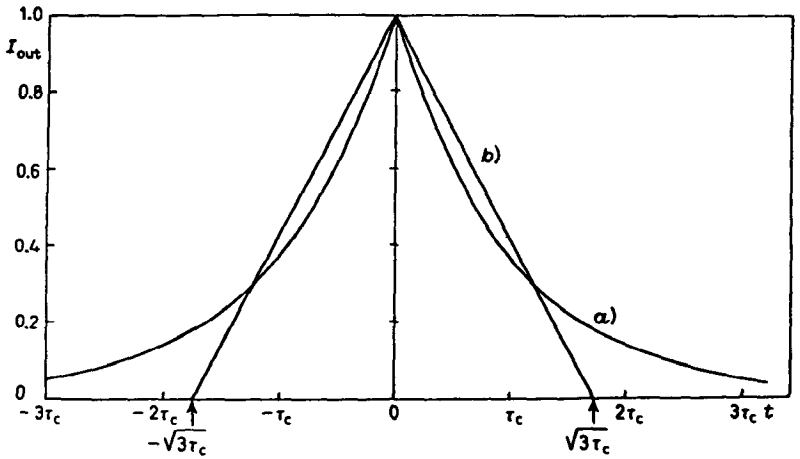

Figure 8 Impulse response $h(t)$ of (*a*) the optimum filter for the amplifier (series) white noise and a (parallel) white noise current at the detector electrode, as in Figure 7. The filter requires a long time to respond. (*b*) Triangular impulse response of optimum width. The noise is higher by only 8% compared with the ideal filter. The width of both responses is determined by the noise corner time constant τ_c. The time of the amplitude measurement (peak of the response) is at the origin.

constrained to a triangular impulse response, its optimum half-width is $(3\tau_c)^{1/2}$, and the noise calculated from Equation 49 is only 8% higher than for the ideal filter.

We usually strive to reduce the parallel noise since it is a result of imperfections and not intrinsic as is the noise associated with the amplification. To reduce the series noise contribution, R_s (i.e. the equivalent series noise voltage) should be as low as possible. To reduce the parallel noise contribution, the equivalent parallel resistance should be as high as possible (since $\langle i_{np}^2 \rangle \propto R_p^{-1}$). In the system design, it is best to make the noise corner time constant τ_c much longer than the system response. Then the second term in Equation 49 becomes negligible. It can be shown that the optimum response for the series (amplifier) noise alone is a triangular function,

$$h(t)\begin{cases} = 1-|t|/t_m & \text{for} \quad |t| < t_m \\ = 0 & \qquad\quad |t| > t_m, \end{cases} \qquad 51.$$

where t_m is the zero-to-peak time (and the FWHM) and it defines the measurement time with respect to the time of occurrence of the signal impulse. The first integral in Equation 49 is $2/t_m$ for this triangular function, and the equivalent noise charge for the series noise is

$$\mathrm{ENC}_s^2 = 4kTR_s \frac{C_{in}^2}{t_m}. \qquad 52.$$

In terms of transistor parameters $\tau_A = C_{GS}/g_m$ and a_n (Equations 37, 45, 46), it can be expressed as

$$\mathrm{ENC}_{s\,opt}^2 = 4kTa_nC_D[(C_D/C_{GS})^{1/2} + (C_{GS}/C_D)^{1/2}]^2\tau_A/t_m, \qquad 53.$$

where τ_A approaches the electron transit time t_{el} for an ideal device where parasitic capacitances and resistances are neglected. The term in brackets is a measure of the capacitance mismatch between the transistor and the detector electrode (with connections). This term has a minimum for $C_{GS} = C_D$. The theoretical lower limit for the noise achievable with field-effect devices ($a_n = 2/3$) is then

$$\mathrm{ENC}_{s\,opt} = 4(2/3)^{1/2}(kT)^{1/2}C_D^{1/2}(\tau_A/t_m)^{1/2} \qquad \text{for } C_{GS} = C_D. \qquad 54.$$

Assuming state-of-the-art amplifier devices with $\tau_A = C_{GS}/g_m \approx 0.5$ ns, we obtain $\mathrm{ENC}_{s\,opt} \approx 30$ rms e for the following pairs of values of the detector capacitance C_D and the measurement time t_m: 0.1 pF at 100 ns, 1 pF at 1 μs, 10 pF at 10 μs, etc.

NOISE AND SIGNAL "ENERGY" It is interesting to compare the amplifier (series) noise and the parallel noise from the point of view of energy and the equipartition theorem. The amplifier noise energy referred to the input capacitance $C_{in} = 2C_D$ for $C_{GS} = C_D$ is from Equation 54,

$$\mathrm{ENC}_s^2/2C_{in} = (8/3)kT\tau_A/t_m. \qquad 55.$$

The capacitance $C_D + C_{GS}$ in Figures 5 and 7 is a system with one degree of freedom, and it has by the equipartition theorem from statistical thermodynamics a thermal noise energy $kT/2$. This represents the total fluctuation energy for all frequencies. The amplifier noise is much lower because the pulse-shaping filter restricts the frequency band in which the signal and the noise are measured. The ratio t_m/τ_A is typically in the range 10^2 to 10^4 for particle detectors, so that the amplifier apparent noise energy is much lower than $kT/2$. The thermal noise on the capacitance is generated by the dissipative components in the input circuit represented by the parallel resistance R_p in Figure 7. The extent to which this noise affects the measurement is determined by the relation of the measurement time t_m to the noise corner time constant τ_c, Equation 49. For $\tau_c \gg t_m$, this noise is at frequencies much lower than the frequency response of the pulse shaping. The signal energy on the input capacitance is $Q_s^2/2C_{in} = Q_s^2/4C_D$, so that the ratio of the signal energy to the amplifier noise energy is inversely proportional to the detector capacitance. The role of the electron transit

time in the amplifying device is to determine the lower limit of the device time constant $\tau_A = C_{GS}/g_m$ and thereby the noise.

THE PULSE SHAPING The role of "pulse shaping," "signal filtering," or "signal processing" is to minimize the measurement error with respect to the noise, and at high counting rates to minimize the effects of pulse overlap or pileup. The term "pulse shaping" implies that the amplifier-filter system is time invariant. In such a system there are no variations with time in the system parameters during the measurement, and a single measurement of amplitude or time is performed. Such a system is described completely by its impulse response.

In signal filtering, we also use time-variant methods, such as capacitor switching and multiple sampling of the signal. The filtering properties of a time-variant system are described by its weighting function $w(t)$. The weighting function describes the contribution that a noise impulse, occurring at time t, makes at the measurement T_m, as illustrated in Figure 7. It is essentially a measure of the memory of noise impulses (or any other signals) occurring before the observation time T_m. As shown in Figure 7, the weighting function for time-invariant systems is simply a mirror image in time of the impulse response. For a time-variant system, the impulse response (output waveform) is generally quite different from its weighting function. Time-invariant and time-variant processing can be devised to produce the same result, i.e. both methods will be described by the same weighting function, while their implementation will be quite different. The noise-filtering properties of any weighting function for the two types of noise are described by the following two integrals:

the *series noise integral*:

$$I_1 = \int_{-\infty}^{\infty} [w'(t)]^2 \, dt = a_{F1}/\tau_F \, [s^{-1}], \tag{56.}$$

the *parallel noise integral*:

$$I_2 = \int_{-\infty}^{\infty} w^2(t) \, dt = a_{F2}\tau_F \, [s]. \tag{57.}$$

We may use the impulse response $h(t)$ for time-invariant systems in these integrals, as was done in the derivation of noise relations in Equations 47–49. However, only the weighting function $w(t)$ must be used for time-variant systems. The constants a_{F1} and a_{F2} are dimensionless form factors of the weighting function, and are determined from I_1 and I_2 in relation to the time width parameter τ_F. (The choice of τ_F is arbitrary, e.g. zero-to-peak time t_m or total length t_F of the function can be chosen, then $a_{F1} = I_1 t_m$,

etc.) The effect of various parts of a weighting function on the two basic types of noise in charge amplifiers is illustrated in Figure 9. The series noise integral emphasizes that steep parts of the function contribute most of the noise. The parallel noise increases with the length of the response.

From the discussion of the functions in Figure 8, we can surmise that the exact shape of the weighting function is not important (except for the last ~10% from the optimum value) to achieve a low-noise performance. For example, a gaussian weighting function gives about the same value for the series noise (integral I_1) as a triangular function in Figure 8 of equal FWHM, and its parallel noise is only 6% higher. In practice, weighting functions may have to satisfy some other criteria. If the charge collection time in the detector (induced current duration) is not negligible compared to the length of the weighting function (as it should be for the functions in Figure 8), the function will have to be broader at the maximum to provide a constant weighting for the signal (a flat or rounded top as in Figure 9). The function may also be bipolar with area balance, which is necessary to avoid baseline shifts.

A typical unipolar and bipolar impulse response realized with time-invariant filters is illustrated in Figure 10. This type of response is realized with several resistance-capacitance (RC) integrations and with one and two differentiations, respectively. It has been used with a variety of detectors on different time scales. If the unipolar response is nearly optimized for a signal amplitude measurement, its derivative is an optimum function for the timing measurement. The timing measurement is performed at the zero crossing, and the timing is independent of the signal amplitude. The

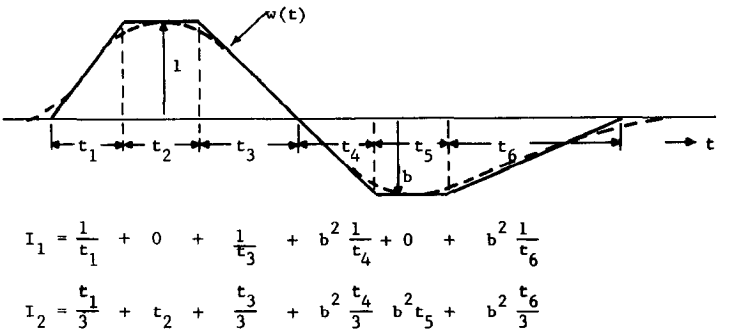

Figure 9 An illustration of the effect of signal processing on the noise in charge measurements. Contributions by the weighting function (impulse response) to the series noise integral I_1 and the parallel noise integral I_2 (Equations 56, 57) are indicated approximately for each segment of the function.

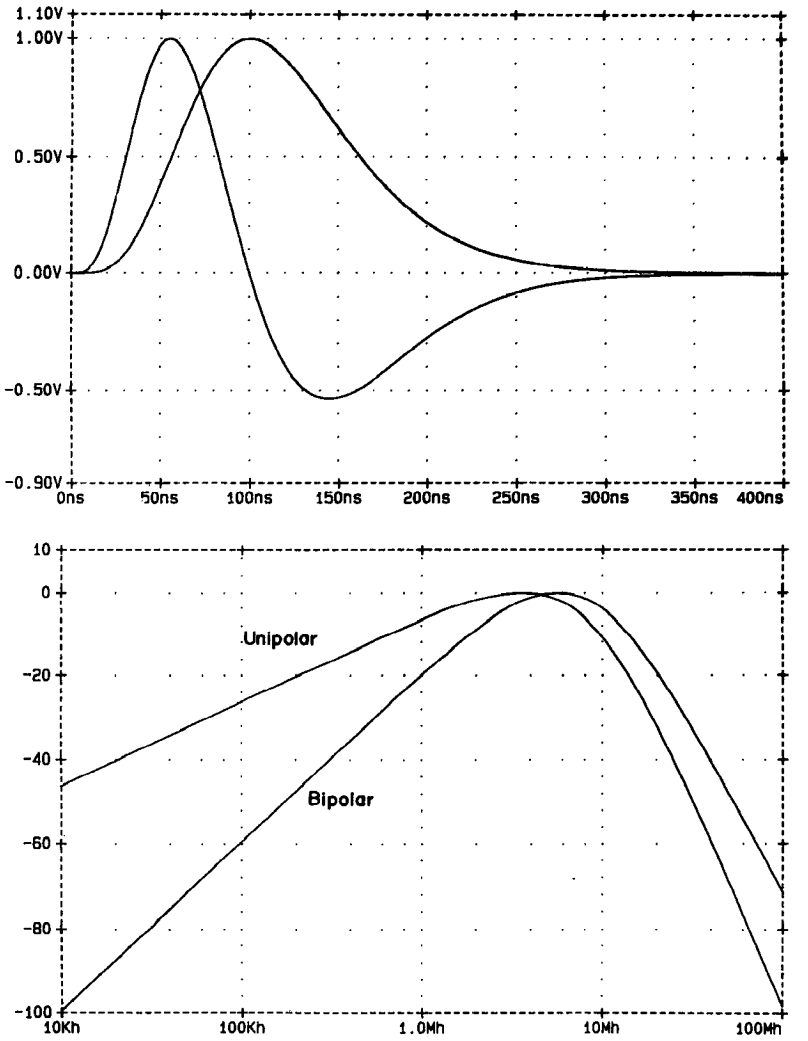

Figure 10 Commonly used functions for unipolar and bipolar pulse shaping (*top*) and their frequency response (*bottom*). The unipolar response is achieved with 5 RC integrations and 1 RC differentiation, with RC = 20 ns. The bipolar response is due to 4 RC integrations and 2 RC differentiations (equivalent to a mathematical differentiation of the unipolar response). The noise integrals, $I_1 = a_{F1}\tau_F^{-1}$ and $I_2 = a_{F2}\tau_F$ (Equations 56, 57), form factors a_{F1} and a_{F2}, and τ_F = FWHM (approximately equal to zero-to-peak time) are:

	τ_F [ns]	I_1 [s^{-1}]	I_2 [ns]	a_{F1}	a_{F2}
unipolar	105	2.2×10^7	80	2.3	0.76
bipolar	52	6.2×10^7	58	3.2	1.1

Vertical scale for the frequency response is in decibels (20 db = factor of 10 in amplitude).

frequency response of these two filters is also shown in Figure 10. The value of the series noise integral is higher for the bipolar function, and its shorter rise time corresponds to increased response at high frequencies compared to the unipolar function. The parallel noise integral is higher for the unipolar function, corresponding to increased response at low frequencies.

4.3 *Sources of Noise in Charge Amplifiers*

The simplified picture of the noise in charge amplifiers presented so far is useful to understand the principles, but as is often the case a more complete picture requires many details to be filled in. We address some of the more detailed properties in this section. Various noise sources can be grouped by their location in the circuit and by their frequency spectrum, as shown in Figure 11.

SERIES WHITE NOISE As seen in Sections 4.1 and 4.2, a lower limit for this type of noise is given by the electron transit time t_{el}, and in practice by the device time constant $\tau_A = C_{GS}/g_m$, which may include some parasitic capacitances and resistances. This limit provides a satisfactory measure of performance for devices with a longer channel, for example, state-of-the-art JFETs with $L \approx 7$ μm and $\tau_A \approx 0.5$ ns. As the channel length is decreased, various "short-channel" effects become important. The saturation of the electron drift velocity is associated with an increase in their

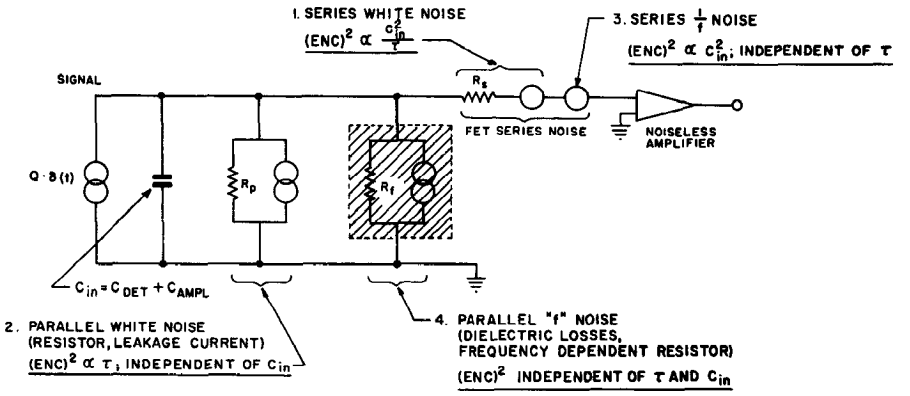

Figure 11 Basic noise sources in the detector-amplifier circuit. The dependence of the equivalent noise charge (ENC) on the pulse-shaping (measurement) time τ (also τ_F and t_m in the text) and on the capacitance C_{in} is indicated. The parallel white noise integrated on C_{in} results in a $1/f^2$ spectrum at the amplifier input. The noise current due to dielectric losses with an "f" spectrum (63, 64), integrated on C_{in} results in a $1/f$ spectrum at the amplifier input.

temperature, and such hot electrons generate additional noise by increasing channel noise and by creating a current between the channel and the gate produced by impact ionization (63). The gate leakage current acts as a source of parallel noise since it flows into the input capacitance. The series resistance at the source results in a larger reduction of the transconductance with a short channel. The optimal channel length, which gives minimal channel thermal noise, has not been established in JFETs. Shorter channels are easier to realize in MOS technology. However, a MOSFET with a channel length of $L \approx 3$ μm is not necessarily better than a JFET with $L \approx 7$ μm. MOS devices have a higher $1/|f|$ noise (see below). The p-channel MOS devices are better than the n-channel devices in this respect. The majority carriers (holes) in a p-channel MOS device have a much lower mobility in the inversion layer compared to electrons in a JFET channel, so that the improvement is much less than might be expected from the ratio of the channel lengths.

A scanning electron micrograph of a typical JFET is shown in Figure 12. Devices of this type are made in different channel widths (dimension W in Figure 5) while keeping the same channel length L. In this way, the capacitance C_{GS} of the device can be matched to the detector capacitance, C_D, while the device constant $\tau_A = C_{GS}/g_m$ remains the same. From Equation 5 the increase in noise due to the capacitance mismatch is,

$$\mathrm{ENC_s/ENC_{s\ opt}} = \tfrac{1}{2}[(C_D/C_{GS})^{1/2} + (C_{GS}/C_D)^{1/2}]. \qquad 58.$$

For a moderate mismatch (by a factor of 5), the noise increase is $\mathrm{ENC_s/ENC_{s\ opt}} = 1.34$, but for $C_d/C_{GS} = 100$, the noise increases by a factor of ~ 5. Large-area devices with a capacitance C_{GS} in the range of several hundred picofarads have been built (Interfet Corp., Garland, Texas). Matching of high capacitance detectors without an impractical increase in the device size and power dissipation can be achieved with a transformer (2).

With bipolar transistors, lower values of the device time constant have been achieved than with JFETs or MOSFETs (20–50 ps, with some experimental devices around 10 ps). The main discrepancy from the noise model (Equations 42, 44, 54) is the thermal noise in the base-spreading resistance $r_{bb'}$ (between the base contact and the active region of the base). The equivalent series noise resistance for the bipolar transistor is then, with Equation 45,

$$R_s = r_{bb'} + 1/(2g_m). \qquad 59.$$

In larger discrete devices, $r_{bb'}$ is usually less than $\sim 30\ \Omega$, while in small, high-speed devices in monolithic technology it can be as high as 200 Ω. In comparison to $(2g_m)^{-1} \approx 40\ \Omega$ at $I_c \approx 1/3$ mA, the base resistance may

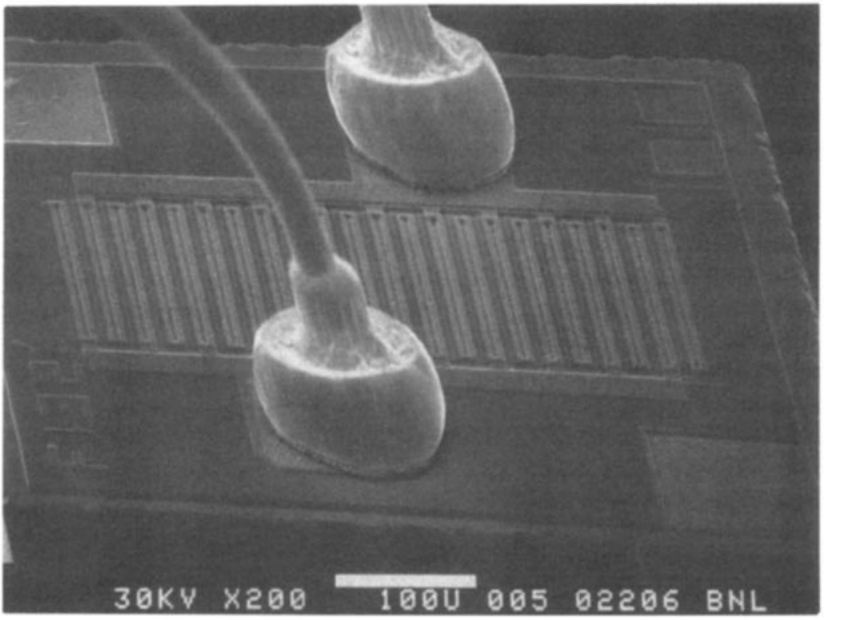

Figure 12 Scanning electron micrograph of a silicon junction field-effect transistor (type 2N6451 by Interfet Corp., Garland, Texas) commonly used in charge amplifiers for particle detectors (e.g. liquid argon ionization chambers). The number on the chip (F132) designates the channel width (W in Figure 5) in thousands of an inch ($\sim$3.3 mm in this example), and it determines the transconductance and the gate-to-source capacitance, $g_m \approx 20$ mS and $C_{GS} \approx 12$ pF. The device time constant $\tau_A \approx C_{as}/g_m \approx 0.6$ ns is determined by the channel length and is proportional to the spacing between the source and drain contact fingers. Bonded contacts for source and drain are shown. The top gate is connected to the bottom gate on the chip.

increase the series noise significantly. The input (diffusion) capacitance of the bipolar transistor is proportional to the collector current as is g_m (Equations 44 and 42) so that the capacitance matching to the detector can be realized over a limited range by varying the collector current.

PARALLEL WHITE NOISE The importance of the parallel noise depends on the time scale of the measurement in relation to the noise corner time constant, Equation 49. It is illustrative to find the optimal shaping time for which series noise equals parallel noise. For series noise $ENC_s \propto t_m^{-1/2}$ and for parallel noise $ENC_p \propto t_m^{1/2}$. By setting ENC_s equal to ENC_p and by using Equations 47, 51, and 54 for $C_{GS} = C_D$ with Equations 22, 24, and 27, we obtain for the bipolar transistor collector current (series) and base current (parallel) noise

$$t_{m(opt)} = 2 \times 6^{1/2} h_{FE}^{1/2} \tau_A. \quad 60.$$

For a transistor with a current gain $h_{FE} = 100$ and a device time constant $\tau_A = 100$ ps, the minimum noise ENC $= 2^{1/2}$ ENC$_s$ is achieved for $t_{m(opt)} \approx 5$ ns, where t_m is zero-to-peak time of a triangular weighting function. Obviously, bipolar transistors are best for fast detectors and short measurement times; their use at longer measurement times is limited by the base current shot noise. With field-effect devices, the gate leakage current is sufficiently low that the series noise is dominant for t_m of up to 10 μs or more.

1/*f* NOISE Silicon MOS field-effect transistors and gallium arsenide metal-semiconductor field-effect transistors (MESFETs) are known to have a relatively high $1/f$ noise compared to silicon junction FETs and bipolar transistors. This $1/f$ noise appears as fluctuations in charge in the gate-channel interface, which modulate the conducting channel. How some distributions of time constants in the charge trapping-detrapping process in SiO_2 may lead to a noise with $1/|f|$ power spectrum is described in (58). The noise that modulates the conducting channel appears as an equivalent voltage generator in series with the control electrode (gate), as indicated in Figure 11, with a spectral density of

$$\langle v_{1/f}^2 \rangle = A_f |f|^{\alpha}, \quad 61.$$

where A_f [V^2] is a constant for $1/f$ noise determined for each device as $\langle v_{1/f}^2 \rangle |f|^{-\alpha}$ at any frequency where Equation 61 is valid. A_f is inversely proportional to the device area (width W in Figure 5). The exponent α is usually between -0.8 and -1.2. This relation has been found over many decades to hold to very low frequencies for MOS transistors.

The equivalent noise charge for $1/f$ noise is independent of the filter-shaping time and it is only weakly dependent on the shape of the filter-weighting function (58). This is because integration of the $1/f$ spectrum over the frequency band f_{low} to f_{high} gives an rms value $\sim [\ln (f_{high}/f_{low})]^{1/2}$, and the ratio f_{high}/f_{low} is independent of the time scale parameter τ_F (or t_m) of the filter-weighting function.

The equivalent noise charge for series $1/f$ noise for filters commonly used with radiation detectors is given by the approximate relation (38, 64)

$$ENC_{1/f}^2 \approx 4(A_f C_{GS}) C_D [(C_D/C_{GS})^{1/2} + (C_{GS}/C_D)^{1/2}]^2. \quad 62.$$

Any series device noise is minimized for $C_{GS} = C_D$,

$$ENC_{1/f\,opt}^2 \approx 16(A_f C_{GS}) C_D. \quad 63.$$

$A_f C_{GS}$ is independent of the device area (width W) and it is a measure of $1/f$ noise "energy" in joules. It depends on the design and technology of

the device, and it is a function of the oxide thickness in MOS device. It is interesting to determine the "corner" measurement time t_{mc} at which the device intrinsic white noise and the $1/f$ noise contribute equally to the equivalent noise charge. From Equations 53 and 63, we obtain

$$t_{mc}/\tau_A = (2/3)kT/(A_f C_{GS}). \quad 64.$$

Thus the ratio of the "corner" measurement time and device time constant is determined by the ratio of the channel thermal noise energy to the $1/f$ noise energy constant. We can similarly determine the "corner" frequency f_c at which the equivalent series noise spectral density is equal for these two sources,

$$f_c = (4t_{mc})^{-1}$$

$$f_c\tau_A = (3/8)(A_f C_{gs})/kT. \quad 65.$$

Since $ENC_s \propto t_m^{-1/2}$ and $ENC_{1/f}$ is independent of t_m, $1/f$ noise dominates for $t_m > t_{mc}$.

In silicon junction FETs and bipolar transistors $1/f$ noise is very low, with $A_f C_{GS}$ in the range of 10^{-26} J or less. This represents a contribution to the equivalent noise charge of only ~ 2.5 rms electrons and $t_{mc} \approx 130$ μs for $C_D = 1$ pF and $\tau_A \approx 0.5$ ns. For MOS devices, the constant $A_f C_{GS}$ has been observed to be several orders of magnitude higher. For example, for $A_f C_{GS} \approx 10^{-23}$ J, $ENC_{1/f\,opt} \approx 80$ rms electrons, and $t_{mc} \approx 130$ ns. A discrete MOSFET and a monolithic MOSFET on a CCD exhibited a lower value of $A_f C_f$ in the range of 5×10^{-25} J, and t_{mc} values in the range of ~ 2 to 5 μs have been observed.

Gallium arsenide field-effect transistors (MESFETs) and modulation doped transistors (MODFETs) developed for use at microwave frequencies, would appear to be very attractive as charge amplifiers, in terms of the fundamental limits as expressed by the electron transit time t_{el} and the device time constant τ_A (Equations 37, 46, 54). Electron transit times through a channel of 0.5 μm, in the range of 5 ps, and an $f_T \approx 90$ GHz have been achieved. However, the $1/f$ noise in these devices extends to f_c values of 100 MHz or more. These devices also have high gate leakage currents, which results in high parallel noise. This restricts the usefulness of GaAs devices at their present state of the art to the range below a few nanoseconds.

NOISE IN DIELECTRICS Thermal fluctuations in dielectrics generate a noise the magnitude of which is quantitatively related to the parameters describing dielectric losses. This type of noise has been studied in (63, 64); we present here only the result. For a dielectric with low losses, the dissipation factor or the loss factor D (equal to the imaginary part ε'' of the permitivity

$\varepsilon = \varepsilon' + j\varepsilon''$) is independent of frequency in the range of interest here ($\sim 10^4$ to 10^8 Hz). It can be determined as $D = G(\omega)/(\omega C_d)$, where $G(\omega)$ and C_d are the loss conductance and the capacitance of the dielectric as measured on an impedance bridge at an angular frequency ω. It can be shown that the dissipative dielectric acts as a source of $1/f$ noise in parallel with the detector and the amplifier input (Figure 11). The equivalent noise charge (63, 64) is given by

$$\mathrm{ENC}_d^2 \approx 2.4kTDC_d, \qquad 66.$$

and, as is characteristic for $1/f$ noise, it is independent of the pulse-shaping time. The noise in dielectrics may be very significant with some detectors. If a capacitance of 1 pF is present with a dissipative dielectric, such as fiberglass circuit board with $D \approx 2 \times 10^{-2}$, this alone contributes $\mathrm{ENC}_d \approx 86$ rms electrons to the equivalent noise charge of the detector-amplifier. Best dielectrics (e.g. Teflon, polystyrene, quartz) have $D \approx 5 \times 10^{-5}$ to 10^{-4}, which results in $\mathrm{ENC}_d \approx 5$ to 12 rms electrons.

NOISE SOURCES—SUMMARY AND DISCUSSION A summary of the noise, due to all the sources described here for some typical detectors and amplifying devices, is given in Figure 13 over a wide range of detector capacitances

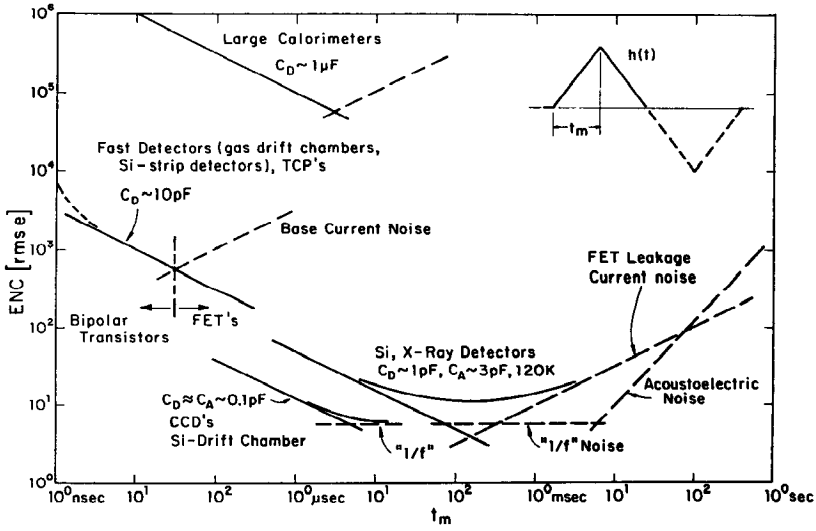

Figure 13 The equivalent noise charge as a function of the measurement time for various detectors (orientative values). Various noise components exhibit characteristic dependence: for the amplifier intrinsic noise $\mathrm{ENC}_s \propto t_m^{-1/2}$ (*solid lines*); for parallel white noise (from detector leakage currents, transistor base current, and resistors at the input) $\mathrm{ENC}_p \propto t_m^{1/2}$ (*dashed lines* with $t_m^{1/2}$ slope); for the series and parallel $1/f$ noise, $\mathrm{ENC}_{1/f} \propto$ constant (*horizontal dashed lines*).

and pulse-shaping (measurement) times. We note that for the series noise $ENC_s \propto t_m^{-1/2}$, for the parallel noise $ENC_p \propto t_m^{1/2}$, and for the $1/f$ noise $ENC_{1/f} \propto t_m^0$. The parallel white noise current is integrated on the input capacitance and it becomes $1/f^2$ noise (in voltage and charge), as discussed in Section 3.2. Thus, we have at the input the amplifier (series) white noise, series and/or parallel $1/f$ noise, and $1/f^2$ noise from parallel (white sources). The general connection between the exponent α for a noise with a power-law spectrum $|f|^\alpha$, Equation 30, and the equivalent noise charge is then (58)

$$ENC^2(\alpha) \propto t_m^{-(1+\alpha)}. \qquad 67.$$

A measurement of the total system noise ENC versus t_m and C_{in} may allow decomposition into several basic power-law noise components (where α does not have to be an integer) and provide an insight into the sources of noise. Such analysis is customary in experimental studies of noise in charge amplifiers (37, 39, 64).

The curves for the silicon x-ray detectors and for the CCD in Figure 13 are for operation of the detectors and the input field-effect transistors at low temperatures ($\sim$120–170 K). The thermal noise in resistors and dielectrics is reduced according to Equations 27 and 66. The thermally generated leakage currents are reduced, and so is their shot noise. The maximum reduction in the thermal (series) noise of field-effect transistors is about 30% at temperatures in the range of 120–160 K. The dependence of the noise in JFETs on temperature is discussed in (10, 23).

Are there any other ways to detect and amplify charge signals than by the field-effect or bipolar transistor action? A parametric charge amplifier was developed in 1964 (65) just before the technology of low-noise field-effect transistors was developed. The parametric amplifier makes use of the charge (and voltage) dependence of the capacitance of the reverse-biased pn junction (i.e. variable capacitance diode). It is based on a fairly complex circuit, and it offers no advantage over a simple amplifier with a field-effect transistor at room temperature. The parametric amplification may attain a lower noise at very low temperatures (<4 K).

The behavior of various noise sources is described in this review in the context of the detector as a capacitive source of charge. Thermal detectors or bolometers, demonstrated recently as high-resolution x-ray detectors, are resistive or dissipative signal sources, and the effects of various noise sources are somewhat different (66).

5. DETECTORS AND SIGNAL PROCESSING

The optimal choice of the amplifying device, its operating conditions, the preamplifier circuit, and the pulse shaping depends strongly on the type

of the particle detector, the purpose of the measurement, and in particular, on the signal waveform, the electrode capacitance, and the counting rate. To provide an insight into the interplay of various factors, we discuss briefly some aspects of the signal processing for three types of detectors that are now of great interest in particle physics.

5.1 *Proportional and Drift Chambers*

The signal processing for gas proportional and drift chambers is illustrated in Figure 14. Two types of charge preamplifier circuits are shown with their most essential circuit components. Each preamplifier is best suited for a certain range of pulse-shaping times.

The feedback configuration allows the ultimate in the noise at shaping times longer than about 50 ns because the parallel noise sources can be made negligible by using a field-effect transistor (with a gate leakage current in the pA range) and a very high feedback resistance (megaohms to gigaohms). (The feedback resistor can be avoided altogether by using a switch to maintain the amplifier voltages in the operating range, as shown in the circuit for semiconductor detectors in Section 5.2.) This basic circuit is also used with ionization chamber calorimeters, Section 5.3. Its properties are discussed in some detail in (24, 37, 64).

The common-base input configuration in Figure 14*b* has a very fast

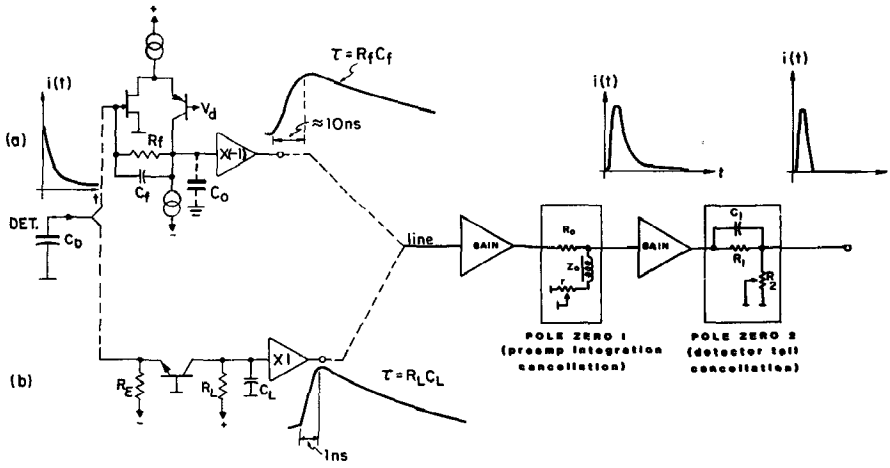

Figure 14 Signal processing for gas proportional, drift, and time projection chambers. The feedback charge amplifier (*a*) with a field-effect transistor (junction or MOS) is for pulse-shaping times $t_m > 30$ ns. The common-base input charge amplifier (*b*) with a bipolar transistor is used at $t_m < 50$ ns. Preamplifier output stages ($\times 1$) contain two cascaded emitter followers. Gain stages in the shaping amplifier include *RC* integrations.

impulse response ($\sim$1 ns rise time) and it is used with very short pulse-shaping times, t_m in the 3–50-ns range. As discussed in Section 4.3, the base current shot noise becomes dominant at longer shaping times.

The feedback configuration is less suitable for very fast response (rise times of less than $\sim$10 ns), because instability of the feedback loop may arise as a result of inductance and propagation time effects in cases where the connections to the detector electrodes are not very short. The detector induced current is integrated on the feedback capacitance C_f in the feedback circuit, and on the capacitance C_L of the collector node to ground in the common-base circuit. The decay in the preamplifier response is due to the discharge of C_f and C_L through the feedback resistance R_f and the collector load resistance R_L, respectively. The long tail in both configurations can be cancelled in the subsequent pulse shaping by simple circuits shown in Figure 14.

Attempts at pulse shaping in the preamplifier by reducing R_f and R_L lead inevitably to an increase in the equivalent noise charge from the thermal noise of these resistors. A primary objective of the detector-amplifier design should be to avoid dissipative components at the input. The noise from the collector load resistor R_L in the common-base configuration is equivalent to that from the resistor R_E in the emitter (since the current gain from the emitter to the collector is unity). The noise in the common-base configuration is discussed in (67).

The pulse shaping consists functionally of two parts. One is the band limiting at high frequencies (RC integrations) and the other is the band limiting at low frequencies (RC differentiations or delay line clipping). For $(n-1)$ integrations and one differentiation with equal time constants $\tau_i = \tau_d = RC$, the impulse response from the input of the preamplifier to the output of the shaping amplifier is a Poisson function of the nth order, $h(t) = (t/\tau_i)^n \exp(-t/\tau_i)$. The zero-to-peak time $t_m \approx$ FWHM of this function is $n\tau_i$. Such a function with one and two differentiations is shown in Figure 10. For very short shaping times, such a function may be obtained naturally by using the transistor capacitances and the collector load resistors without any additional components. The gain stages in the shaping amplifier can be realized by several circuit modules with the same circuit as the common-base preamplifier but with lower values of the resistors R_L and R_E (the noise from R_L and R_E in the shaping amplifier is negligible, since the signal is already amplified by the preamplifier). The capacitance C_L consists of the collector-to-base capacitances of the first and second transistor and of the connection stray capacitances. C_L can be as low as 1 pF in hybrid circuit technology and 0.1 pF in monolithic technology. The R_L is then chosen to achieve the required RC integration time constant, e.g. $R_L C_L \approx 1$ ns for very fast processing with $t_m \approx$ 4–5 ns.

It is interesting to study the power dissipation of the common-base pulse-shaping circuit. We note that as the collector load resistance R_L is increased, the transistor dc (standing) current I_{c0} can be reduced. Since $R_L = \tau_i/C_L$ and $\tau_i \propto t_m$, the power dissipation $P \propto I_{c0} \propto R_L^{-1} \propto C_L/t_m$. (There is also an additional factor, that as R_L is increased, the gain per stage is increased and fewer gain states are needed.) Thus, very fast pulse shaping results in higher power dissipation. It is also apparent that monolithic bipolar technology requires much lower power because of much lower collector node capacitances than the hybrid technology.

Two methods for shortening the preamplifier and the detector response are shown. One is based on the simple property of exponential decay, that $\exp(-t/\tau) - (1 - t_d/\tau)\exp[-(t+t_d)/\tau] = 0$ for $t > t_d$. This is implemented with partial delay line clipping. The delay for very fast shaping is of the order of 1 ns. The other method is based on replacing a long decay time constant by a short one, and it is known as the pole-zero cancellation. (The circuit cost of this method is one resistor, R_1 in Figure 14, since a differentiation with a short time constant C_1R_2 has to be performed in any case.) The differentiated preamplifier response produces a short pulse with an undershot decaying with a (long) time constant τ_L (~ 50 ns for a typical common-base input preamplifier). The undershot is cancelled by adding a fraction of the original signal through R_1. The ratio of the short decay time constant to the long one is R_2/R_1.

The cancellation of the tail in the signal from the gas proportional detector is based on an approximation of the detector single-electron response shown in Figure 2*b*, over a part of the response, by a single exponential function.

The results of the fast pulse shaping outlined here, with a gas proportional detector designed for very high counting rates (68), are shown in Figure 15. A preamplifier with the common-base configuration, a feedback preamplifier, and a fast shaping amplifier, all in hybrid circuit technology, are shown in Figure 16.

NOISE IN DRIFT TIME MEASUREMENTS Drift chambers for high particle multiplicities and high counting rates have small cells and a short drift distance. In such a case we are interested in the drift time measurement on the first ionization cluster (or on a very few clusters). The optimal shaping is then of triangular form with a FWHM $= t_m$ approximately matched to the diffusion spread of ionization electrons during the drift to the anode. We calculate the equivalent noise charge from Equation 52. For a collector current in the input transistor $I_c \approx 330\ \mu$A, the equivalent series noise resistance $R_s \approx 60\ \Omega$ (for a discrete transistor). Assuming $t_m = 10$ ns, and the amplifier and the anode wire capacitance $C_{in} \approx 30$ pF,

we obtain the equivalent noise charge $ENC_s \approx 1.9 \times 10^3$ rms e. We can now estimate the required signal charge from the assumed position resolution $\sigma_x = 100$ μm and the corresponding timing noise $\sigma_t \approx 2$ ns (for a drift velocity of 5 cm μs^{-1}). With diffusion, the signal rise time after pulse shaping may be increased to $t_r \approx 20$ ns. The required minimum signal is then $Q_s = ENC_s t_r/\sigma_t \approx 2 \times 10^4$ e. If this signal is produced by an ionization cluster of two electrons, the effective gas gain should be 10^4. Since we observe only a small fraction (1/5 to 1/4) of the avalanche charge in this short time (Figure 2*b*), the actual gas gain should be 5×10^4, which is moderately high. Thus we find that high-precision drift chambers require the best techniques with respect to the noise and fast pulse shaping.

What can we expect from an integrated circuit version of the preamplifier and the pulse-shaping amplifier in Figures 16*a* and 16*c*? The noise will not be lower because it will be difficult to improve on the present discrete bipolar transistors, with f_T in the range 5–7 GHz, i.e. $t_{el} \approx 25$ ps. The noise may actually be higher because of a higher base-spreading resistance $r_{bb'}$. The monolithic circuit now being developed (69) will have a much lower power dissipation in the shaping amplifier and, of course, a much smaller size.

In time projection chambers (28), the diffusion of electrons is much larger because of long drift distances, and an optimized pulse shaping requires a t_m in the range of 100 ns. This is in the region where the base current shot noise in bipolar transistors is dominant (Figure 13), and the preamplifier with a field-effect transistor gives lower noise.

5.2 *Semiconductor Detectors*

Most of the current effort in the development of semiconductor detectors is concentrated on position-sensitive detectors for high-energy physics. The problem of the detector fabrication and the readout electronics has changed from a single coaxial germanium diode approaching 100 cm^3 in size with one low-noise amplifier used in γ spectrometry to very thin (~ 300 μm) silicon detectors with very large numbers of readout channels (from 10^3 to $\sim 10^5$) for tracking minimum ionizing particles. The developments in these detectors are directed toward reducing the size and power dissipation of the readout electronics and the number of connections by either monolithic integration, or, also, by charge transfer methods in charge-coupled devices (1) and semiconductor drift chambers (36). Some of the readout questions for these detectors are reviewed in (38). We comment here on the noise, the power dissipation in the input device, and the signal filtering.

In a discussion about the noise, we have to distinguish between the expected noise for an ideal device and the acceptable noise in a particular

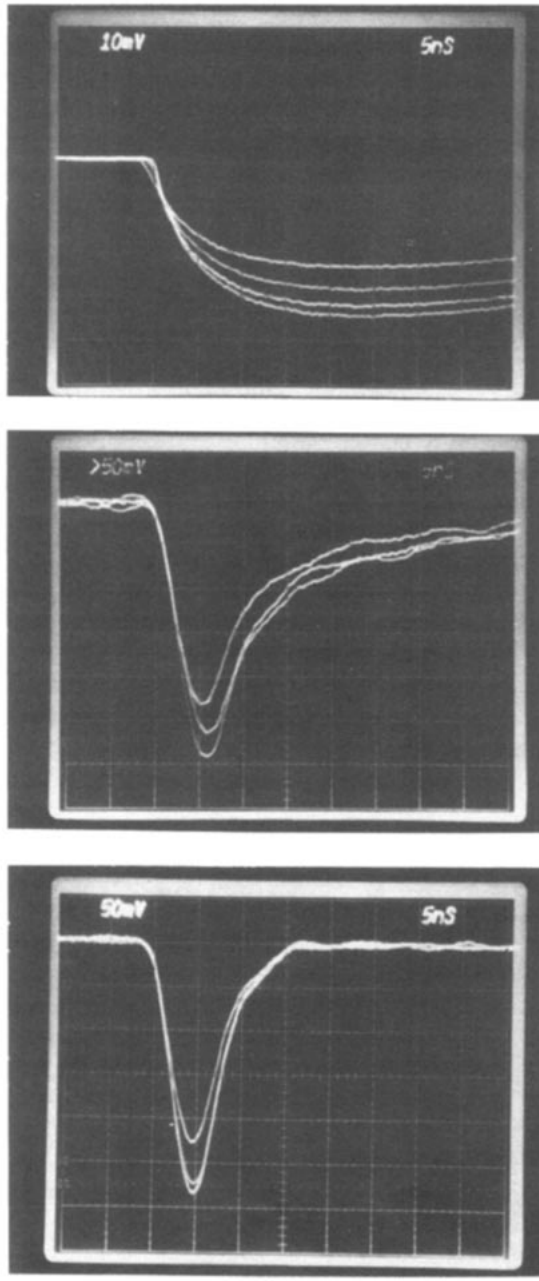

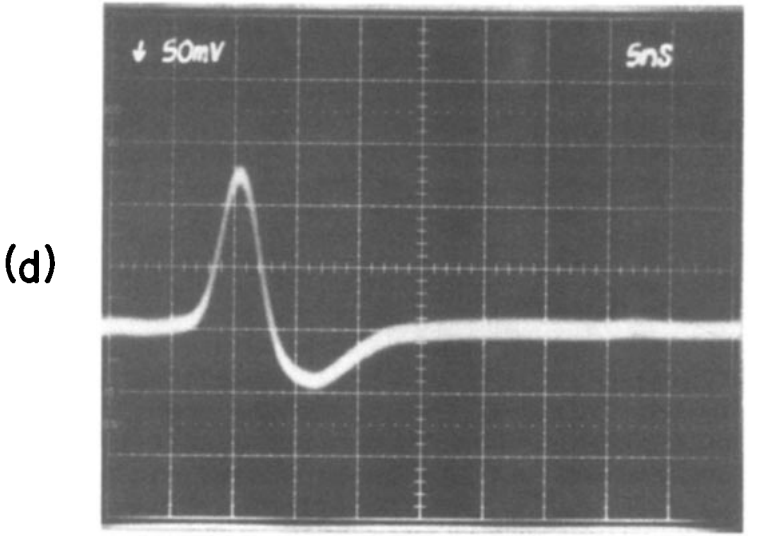

Figure 15 Signals from a fast proportional detector (68) in response to 5.9-keV x rays (point ionization) observed on the preamplifier–shaping amplifier as in Figures 14*b*, 16*a*, and 16*c*. (*a*) Preamplifier output. (*b*) Shaping amplifier output with preamplifier tail cancellation only. This waveform represents the induced anode current in the detector, as in Figure 2*b*. (*c*) The output after detector tail cancellation. (*d*) Impulse response of the preamplifier and the shaping amplifier. Horizontal scale is 5 ns per large division.

application. A higher excess noise may be acceptable for a detector with a very low capacitance (~ 0.1 pF) and not acceptable at higher electrode capacitances (10 pF or more). We may take a junction field-effect transistor as a noise reference, since it approaches (at moderate channel lengths) fairly closely the ideal behavior. In practice $a_n \leq 1$ in Equation 45, which is close to the theoretical value $a_n \approx 2/3$. The MOSFETs in the monolithic charge amplifiers developed so far have a considerably higher noise in both components, the white series noise and the $1/f$ noise, compared to a JFET with an equal device time constant C_{GS}/g_m. The equivalent noise charge has been between 2 and 6 times higher, depending on the device and the measurement time. This has still allowed spectacular results with CCDs, where the values ENC ≈ 6 rms e at $t_m \approx 10$ μs have been observed for $C_D \approx C_A$ in the range 50–150 fF, and the readout MOS transistor is integrated on the device.

The microstrip detectors, illustrated in Figure 17, present a somewhat different problem than the CCDs, since the electrode capacitance is about two orders of magnitude higher ($C_D \approx 10$ pF for a strip length of 5 cm).

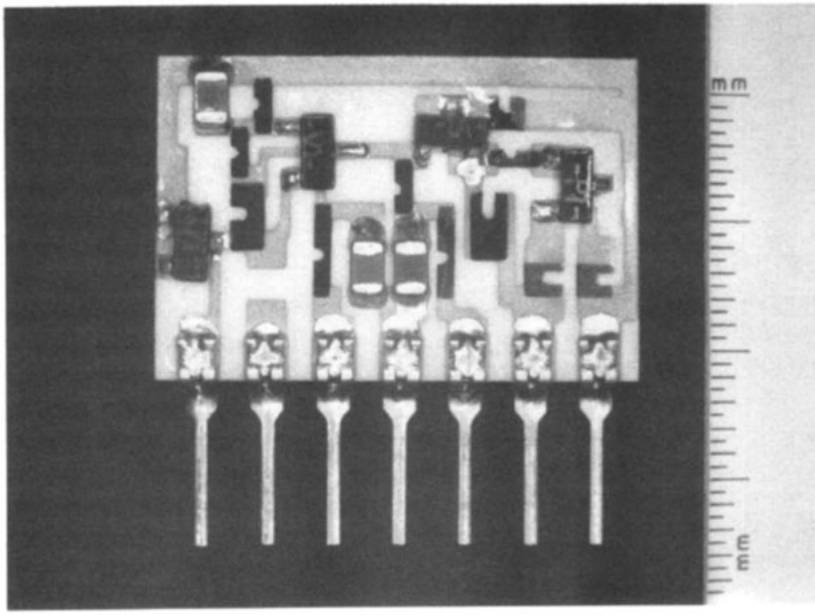

(a)

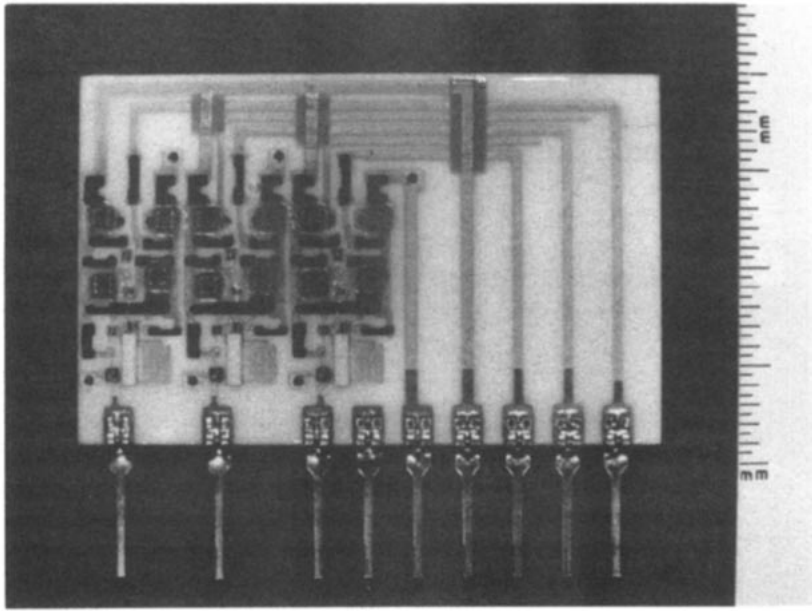

(b)

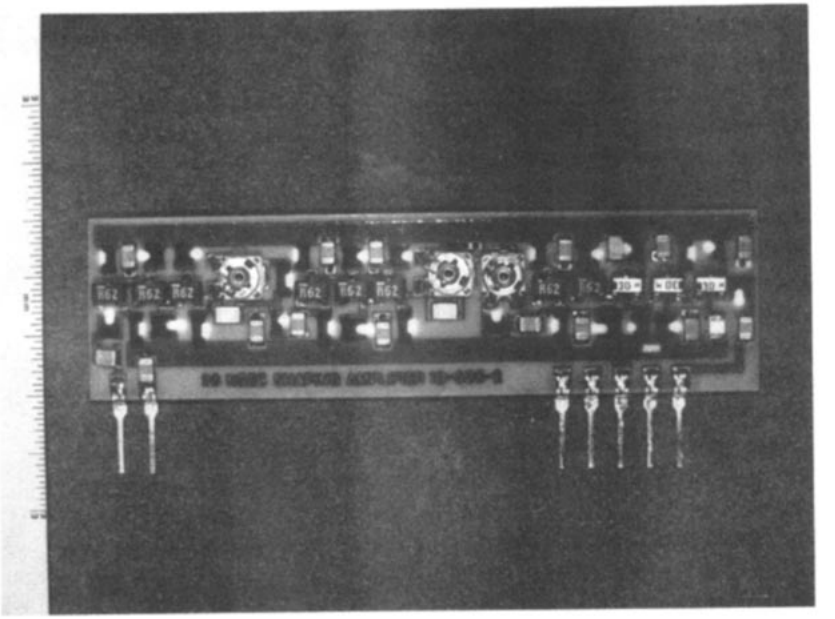

(c)

Figure 16 Hybrid circuit implementation of charge preamplifiers and a fast shaping amplifier. (*a*) The common-base input preamplifier used with proportional and drift chambers and cluster counting (transition radiation) detectors where fast shaping (5–50 ns) is necessary. (*b*) The feedback charge preamplifier (3 channels per board) with a field-effect transistor used with silicon microstrip detectors and on cathode readouts in proportional and time projection chambers. (*c*) The fast shaping amplifier for t_m = 5–50 ns. These are Brookhaven National Laboratory designs, manufactured commercially by REL-LAB, Hicksville, NY 11801 (*a,b,c*) and by Philips Circuit Assembly, New Berlin, WI 53151 (*a*).

There is little quantitative information in the literature on the noise of the monolithic charge amplifiers. An exception is a development at CERN reviewed in (69). The values for ENC in the range of 2000 to 3000 rms e for t_m = 100 to 200 ns have been reported for various designs. While this is marginally acceptable compared to the signal (2.4×10^4 e in 300 μm for Si for a minimum ionizing particle), it does limit the position resolution by interpolation, by any of the methods shown in Figure 17. In comparison, the noise of a junction FET in a hybrid circuit, as in Figure 16, is about 500–700 rms e.

Both the noise and the power dissipation in the device are functions of the drain current. From Equation 37 for field-effect devices we obtain

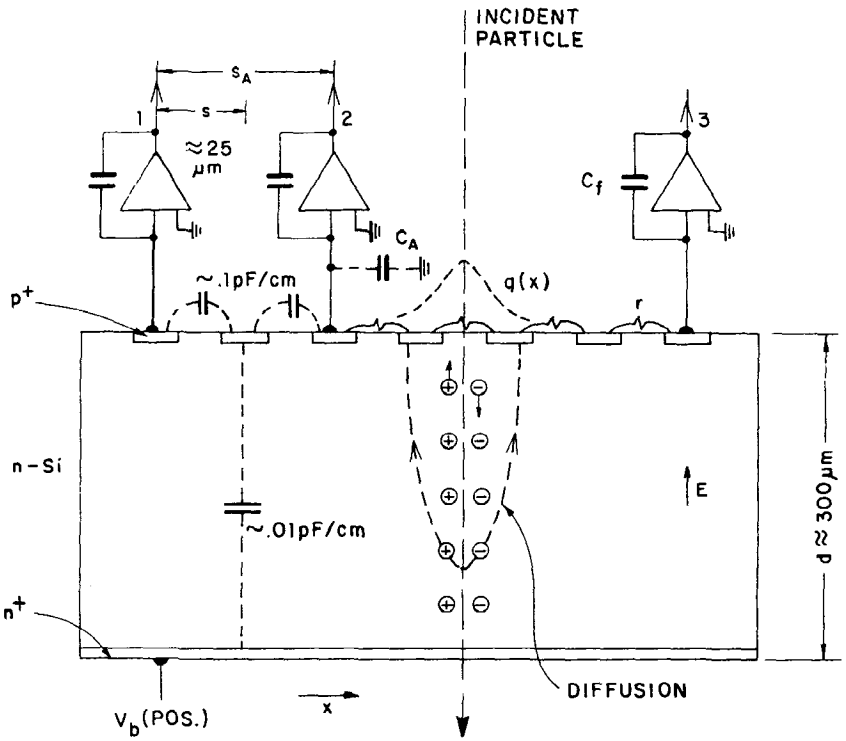

Figure 17 Schematic representation of a silicon microstrip detector and the position readout. Diffusion spreads the charge [distribution $q(x)$] and determines the maximum strip pitch s for linear interpolation. Position interpolation by capacitive charge division (35) is illustrated between amplifiers 1 and 2. Resistive charge division is illustrated between amplifiers 2 and 3.

$$g_m/I_D = 2(V_{GS} - V_T)^{-1}$$
$$g_m/I_D^{1/2} = (2\mu C_{GS}/L^2)^{1/2}$$
$$C_{GS}/g_m = L^2\mu^{-1}(V_{GS} - V_T)^{-1}. \qquad 68.$$

These relations describe the strong inversion condition in MOS devices. We see that for a given device the requirements on the gate bias to achieve a high g_m/I_D ratio (i.e. lower dissipation) and a short device time constant C_{GS}/g_m (i.e. lower ENC) are contradictory. As the current is reduced and the device approaches cut-off $V_{GS} - V_T \to 0$, a region is reached where for all charge-controlled devices the ratio of the transconductance to the current is limited by the thermal (Boltzmann) distribution of carrier energy, $g_m/I_D = e/kT \approx 40\ V^{-1}$ at $T = 293$ K. (This was shown for the bipolar transistor in Section 4.1, Equation 41.) For the field-effect devices, the

device time constant in this region becomes too long. A compromise value is in the range $g_m/I_D \approx 5$–$10\ V^{-1}$.

Integration of the preamplifier and the readout electronics on the same substrate of high-resistivity silicon as the detector presents fabrication processing problems (44). There is little gain in the noise performance by the integration on the detector if the detector electrode capacitance is high and the connections capacitance is negligible. The integration may relieve the bonding problems but would increase the processing and the fabrication problems. The smaller the electrode capacitance, the larger is the benefit in the noise from the integration on the detector since the connections capacitance is avoided. This is particularly important for silicon drift chambers where the charge is collected on very low-capacitance electrodes. A JFET amplifier on high-resistivity silicon is being developed for this purpose (45).

A functional diagram of a multiplexed readout for silicon strip detectors is shown in Figure 18. It is also an illustration of a time-variant signal processing, and of how a unipolar and a bipolar weighting function can be realized by multiple (correlated) sampling. The slope of the function is determined by the rise time of the preamplifier and the amplifier and by the time constant of the switch $S_{1,2,3}$ and the storage capacitance C_m. The operations with the samples shown in Figures 18*c* and 18*d* are exactly equivalent to single and double clipping with delay lines.

5.3 *Ionization Chamber Calorimeters*

Calorimeters are detectors that rely on total absorption to measure the energy of a primary particle. Ionization chamber calorimeters measure the total energy by sampling a fraction of the energy converted into ionization. Sampling ionization calorimeters are based on many plates of a dense material interleaved with small gaps filled with an ionization sampling medium. Liquid argon calorimeters have been used extensively in physics experiments. Organic liquids, which can be used at room temperature, and silicon detectors are being investigated for ionization sampling. Calorimeters are very large devices. They have to surround the interaction region in colliding-beam experiments, and yet their electrodes must be finely subdivided; this creates a large number of electronic readout channels (10^3 to $\sim 10^5$). A large ionization chamber calorimeter represents a giant capacitor, with a capacitance of 1 to 2 μF per cubic meter of the calorimeter volume with liquid sampling media, and one to two orders higher capacitance with silicon. The principles of liquid argon calorimeters and their readout are described in (2), the speed of response and the electronic noise are analyzed in (3), and some readout and pulse-shaping questions in (71). We restrict our brief discussion here to an interesting limitation of the speed of response, to the capacitance matching, and to pulse shaping.

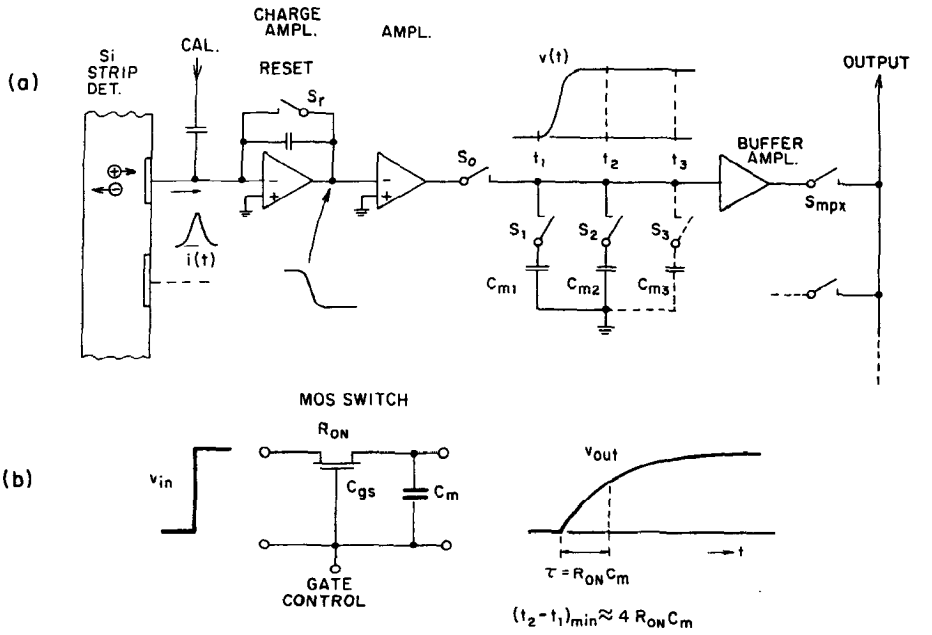

CHARGE TRANSFER TIME In our discussion of low-noise amplification so far, we have tacitly assumed that the connections between the detector electrodes and the amplifying device are short. Thus only the capacitances appear in the equivalent circuits in Figures 5, 7, and 14, and no inductances. This is a sufficiently accurate representation for most detectors, particularly for the noise analysis. In the ionization chamber calorimeters, however, the electrode capacitance of towers or strips connected in parallel for readout by a single amplifier channel is usually in the range of 1 to 10 nF. With these values of the capacitance, the inductance of the connections to the amplifier becomes important. Its effect is to slow down the transfer of charge into the preamplifier. Clearly, the charge measurement cannot be performed until the charge is transferred onto the feedback capacitance of the charge amplifier. The essential components of the chamber-amplifier circuit are shown in Figure 19.

In large calorimeters the amplifiers are typically several meters away from the electrodes connected by a transmission line. A detailed analysis of the charge transfer time is given in (3). An approximate result for the charge transfer time is,

$$t_r \approx 3.5(L_s C_D)^{1/2}, \qquad 69.$$

where L_s is the inductance of the connections, including that of the transmission line, and C_D is the electrode capacitance. The inductance dominates the transmission line effects if the charge transfer time is longer than the propagation time through the line. An electrode capacitance $C_D = 2.5$ nF connected to the amplifier by a 20-ohm transmission line 3 meters long results in a charge transfer time $t_r \approx 150$ ns. Even with amplifiers placed at the chamber electrodes, it becomes difficult to reduce the charge transfer time below about 30 to 50 ns. The minimum width of the overall system response, with bipolar shaping, is about five times longer, $t_f \approx 5t_r$. If we wish to reduce the width of the calorimeter response to 15–20 ns, $(L_s C_D)^{1/2}$ will have to be reduced to ~ 1 ns. This means, for example, electrode sections of $C_D \approx 1$ nF with a connection inductance of $L_s \approx 1$ nH! This limitation is obviously very important for experiments at future accelerators with anticipated very high interaction rates.

Figure 18 An example of time-variant signal processing for silicon microstrip detectors. (*a*) Functional diagram. (*b*) MOSFET switches $S_{1,2,3}$ and storage capacitors $C_{m1,2,3}$ provide *RC* filtering for preamplifier series noise. Signal waveforms on storage capacitors (*left*) and the overall weighting functions (*right*) for (*c*) double sampling and for (*d*) triple sampling. Switch S_r is used for preamplifier reset between the events. Switches $S_{0,1,2,3}$ are closed before the arrival of the event. $S_{1,2,3}$ are opened sequentially to take the samples. During the multiplexed readout, S_0 is open and $C_{m1,2,3}$ are read out sequentially.

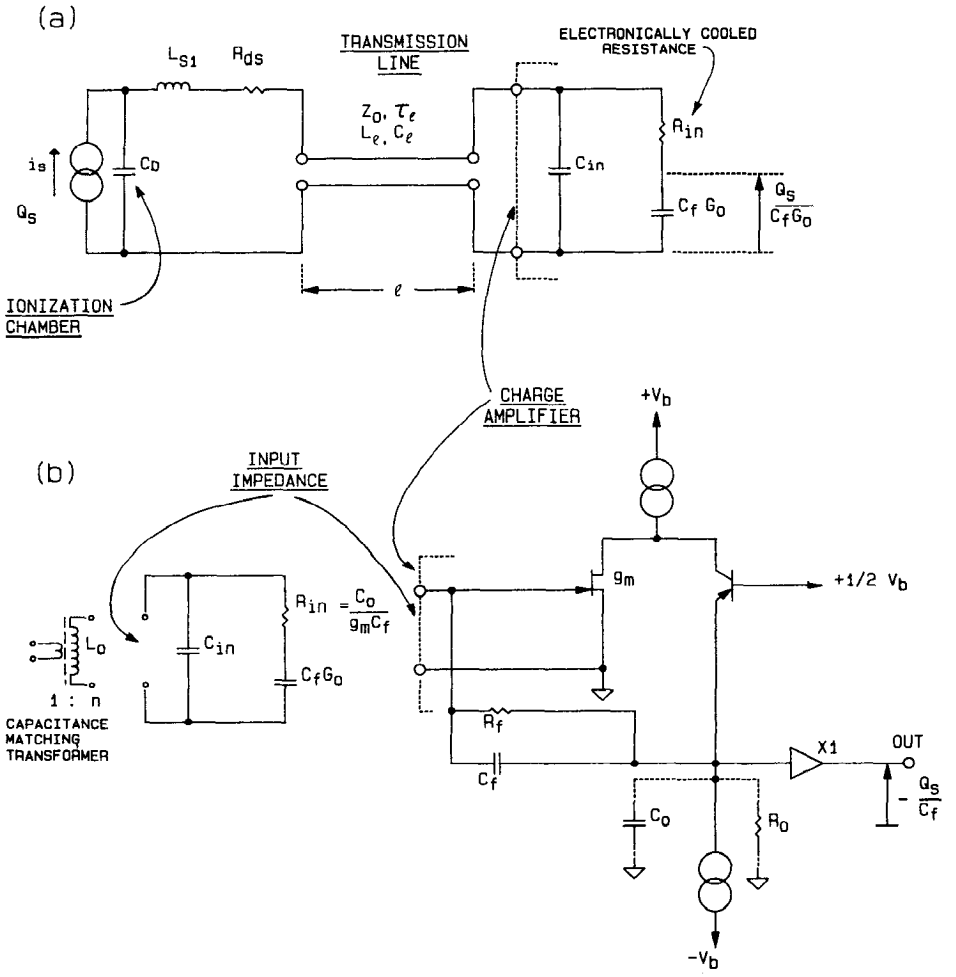

Figure 19 (*a*) The basic chamber-amplifier circuit of ionization chamber calorimeters. (*b*) Charge amplifier configuration and the input impedance in terms of amplifier parameters. Resistive term R_{in} of the input impedance, the "electronically cooled resistance," is essential for the damping of the circuit response (2, 24). C_{in} is a "physical" input capacitance of the amplifier without any feedback effects. $C_f G_0$ is the capacitive term of the input impedance caused by the feedback. $G_0 = g_m R_0$ is the gain at low frequencies (i.e. the "open loop gain").

CAPACITANCE MATCHING With electrode capacitances in the nanofarad range, there is a mismatch between the detector and a typical field-effect transistor ($C_{GS} \approx$ 10–20 pF) by one hundred or more; this results in at least five-fold higher noise than for the matched case, Equation 58. The

matching can be achieved by a signal transformer with a ratio $n = (C_D/C_{GS})^{1/2}$. Transformers of this type are wound on a ferrite core, which precludes their use if the calorimeter is to be operated in a strong magnetic field.

One answer sometimes suggested to the capacitance-inductance question and detector-amplifier capacitance matching is to subdivide the electrodes into small sections and place an amplifier (or just a transistor) on each one of them. In contemplating such a solution, we have to remain aware of the scale of the calorimeter and the numbers involved, as well as of some other problems. An electrode capacitance of 1 μF m^{-3} (or $\sim$50 μF m^{-3} or more for silicon) subdivided in elements of $\sim$100 pF or so would result in tens of thousands of amplifiers per m^3. In liquid media, the protection of these amplifiers against electrical discharges remains an unsolved problem.

A partial solution to the matching problem is to use large-area JFETs, which, in effect, are a parallel combination of devices such as the one in Figure 12, with a capacitance of up to $\sim$500 pF. The transformer still represents the solution with a minimum power dissipation. Matching by a transformer to a low-capacitance device is equivalent to n^2 devices in parallel, but with power dissipation of a single device.

If the signal from the calorimeter is used as a measure of the total energy for the event selection (for trigger purposes), the signals have to be summed linearly from a large part or an entire calorimeter. The equivalent noise charge is then determined by the total capacitance, independently of the number and size of subdivisions, provided that each subdivision is equally matched. The amplifier noise then becomes an important limitation, particularly for short pulse-shaping times.

Could we use MOS transistors for (monolithic) readout circuits in the calorimeter? If we consider the excess noise and a lower resistance of MOS devices to the radiation present in the calorimeter, junction field-effect transistor technology offers a better solution.

A charge amplifier with JFETs has been developed for low-temperature operation inside the cryostat of a liquid argon calorimeter with a fast response. The preamplifiers are at detector electrodes at a temperature slightly above that of liquid argon ("Uranium–liquid argon calorimeter for the HELIOS experiment at the CERN SPS," publication in preparation; details available from author).

CHARGE FEEDBACK AND CAPACITANCE MATCHING We digress here to emphasize the distinction between the transistor control capacitance C_{GS} and the apparent capacitance $C_f G_0$ created at the input of the preamplifier by the charge feedback. The control capacitance should be matched to the detector capacitance (or to the transformed detector capacitance C_D/n^2)

for the best signal-to-noise ratio in an ideal case. One half of the signal charge (i.e. $Q_s/2n$ with a transformer) is then on the amplifying device controlling the output current. The feedback acts equally upon the signal and the noise, and it may affect their amplitudes at various points in the circuit but not their ratio. One role of the charge feedback is to make constant the ratio of the output voltage to the input charge by forcing almost all of the signal charge Q_s onto the feedback capacitance C_f. The other role of the feedback is to provide a resistive component in the amplifier input impedance; this is necessary for damping the detector-amplifier circuit, which includes the inductance of the connections. The components of the input impedance are shown in Figure 19. The damping resistance R_{in} created by the feedback contains the series noise of the amplifying device, which is much less than the thermal noise of a real resistor of equal value. Therefore, it is called an "electronically cooled termination" (2, 3, 24). The signal charge (Q_s/n) is initially deposited equally on $C_{in} = C_{GS} + C_{strays}$ and on C_D/n^2, and then it is transferred onto the feedback capacitance C_f within the preamplifier response time determined by the time constant $R_{in}(C_{in} + C_D/n^2)$. Thus, neither the large capacitance $C_f G_0$ created by the feedback nor the feedback play any role in the capacitance matching.

PULSE SHAPING Some principal properties of signal processing for fast ionization chamber calorimeters are illustrated in Figure 20.

The induced current for liquids, arising from single-carrier charge collection for uniform ionization in the interelectrode gap by shower particles traversing the gap, has a triangular (sawtooth) form (2), as shown in Figure 20*a*. The duration of the current is equal to the electron drift time. A typical bipolar impulse response of the chamber-preamplifier pulse shaping is shown in Figure 20*b*. The most important condition for pulse shaping at high counting rates is that the system impulse response (i.e. the weighting function) have an area balance between positive and negative lobes. With area balance, the pileup does not produce a net shift in the measurement of high-energy events in the presence of a high rate of low-energy background events. The output waveform of the system depends on the relation of the electron drift time t_d to the width of the impulse response t_F. For $t_d \ll t_f$, the output is similar in shape to the impulse response in Figure 20*b*, but broadened by t_d. For $t_d \gg t_F$, i.e. slow charge collection compared to the pulse shaping, the output response becomes a band-limited first derivative of the current pulse, as shown in Figure 20*c*. To obtain an output waveform narrower than the input, one requires an impulse response with three lobes, as shown in Figure 20*d*. The resulting output waveform is shown in Figure 20*e*. There is a small after-pulse (delayed by the electron drift time after

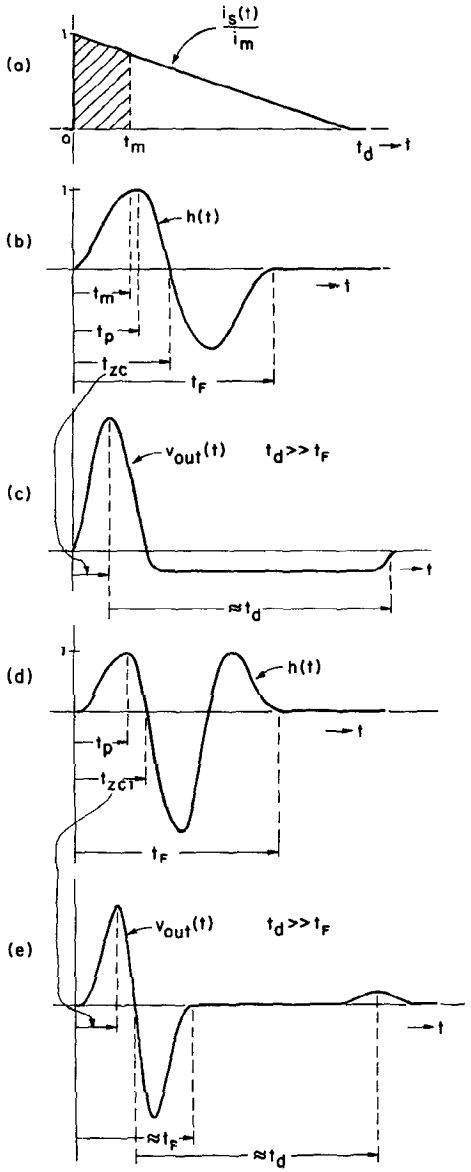

Figure 20 Processing of signals in ionization chamber calorimeters. (*a*) Induced current waveform for ionizing particles traversing the interelectrode gap (single-carrier collection as in liquid media). (*b*) A bipolar impulse response of the detector-amplifier system. (*c*) The output of the bipolar shaping driven by the signal in (*a*) for fast pulse shaping $t_r \ll t_d$. (*d*) A three-lobe impulse response. (*e*) The output of the three-lobe shaping driven by the signal in (*a*) for $t_r \ll t_d$. The term t_d represents electron drift time across the chamber interelectrode gap.

the zero-crossing) caused by the discontinuity at the end of the current pulse. This after-pulse could be removed by a more elaborate impulse response (72). However, its contribution to the pileup is negligible. The weighting functions in Figures 20*b* and 20*d* can be realized also with time-variant filters, based on multiple sampling, similar to those in Figure 18.

We see that, as with gas proportional chambers, we can achieve a signal response shorter than the induced current waveform at the expense of the signal-to-noise ratio (3). A principal limiting factor to the speed of response of ionization chamber calorimeters is the charge transfer time from the detector electrodes to the amplifier.

6. CONCLUDING REMARKS

We have reviewed the gain and noise mechanisms and the limits in charge measurements posed by the noise. We described the equivalent noise charge due to various noise sources in terms of their physical parameters and of the measurement time, to provide an insight into the effects of the noise and into the role of the pulse shaping or filtering. For a given measurement and a signal waveform, and a combination of noise sources, there is an optimum filter-weighting function. We have learned that it is far more important to reduce the noise physically at its source (and not to increase the noise by introducing dissipative components), than it is to realize an optimum filtering function exactly.

There are many methods to realize a weighting function and perform the measurement: time-variant filters with one sample, time-variant filters with one or several samples, and waveform recording where the weighting function is applied in the computer. Any method involving time-variant filters, multiple sampling, or waveform recording requires a careful study of the necessary filtering prior to the sampling and an understanding of the weighting function of the entire system. This is important because the weighting functions for time-variant (e.g. switched capacitance) systems are, in general, not intuitively obvious and certain operations may affect the overall weighting function in such a way as to increase significantly the observed noise.

Why is an understanding of low-noise techniques in particle physics important now? Looking into the future, to experiments in the next two decades (73), it is fairly clear that the trend will continue toward detectors that are still larger, are more sophisticated, and have 10^5 to 10^6 (or more?) electronic readout channels. This will be accompanied by increasing particle energies and interaction rates. The relative energy resolution of the calorimeters and the absolute position accuracy of the tracking detectors will have to improve. High counting rates and particle multiplicities lead

to short pulse-shaping times. All detectors based on avalanche multiplication in gases will have to be operated at a lower gain to reduce space-charge effects, and to extend their operating life at high counting rates. How far we shall be able to go in these directions will be determined to a large extent by the noise in amplifying devices.

The signal processing on such a scale will have to make extensive use of integrated circuit technology. Developments in the fabrication technology have been driven by digital circuit applications. Because of this, the processes are not well suited to linear (analog) circuits, and particularly, not to fast and low-noise circuits (70). The tools for automated analog circuit layout are less advanced than those for digital circuits, and the circuit simulators are often inadequate because they lack good device models. The challenge in the development of readout circuits for particle detectors will be in (*a*) getting access to special processes needed for fast low-noise circuits, (*b*) understanding the device noise behavior, (*c*) undertaking the necessary device development, and (*d*) modeling the devices. We will have to use all three types of silicon devices: bipolar transistors for fast processing in the range of a few nanoseconds, junction field-effect transistors for low-noise and low-temperature operation in the range of 50 ns or more, and MOS transistors for switched-capacitor filters, analog storage, and readout multiplexing. Hybrid technology will be necessary to assemble readout channels consisting of monolithic circuits in different technologies, and occasionally a discrete low-noise transistor.

We can also expect that the best solutions to the more difficult requirements on particle detectors will be found in an integral design of the detector and the readout, where the detector electrodes and the amplifying device parameters are jointly optimized. This natural approach has already been demonstrated in some detectors, and it will be essential in detectors such as silicon pixel detectors, silicon drift chambers, gas detectors for high particle multiplicities, and ionization chamber calorimeters.

ACKNOWLEDGMENTS

The work and ideas reviewed here were stimulated by collaborations and discussions I have enjoyed with many colleagues at the laboratories and universities in the US and overseas. I am particularly indebted to R. L. Chase, C. W. Fabjan, E. Gatti, A. Hrisoho, F. Manfredi, P. Rehak, S. Rescia, H. H. Williams, and W. J. Willis. The amplifiers shown in Figure 16 were designed in hybrid circuit technology by D. Stephani. Finally, I would like to thank B. Gaer for her patient and efficient preparation of the manuscript. This work was supported by the US Department of Energy: Contract No. DE-AC02-76CH00016.

Literature Cited

1. Damerell, C. J. S., et al., *IEEE Trans. Nucl. Sci.* 33: 51 (1986)
2. Willis, W. J., Radeka, V., *Nucl. Instrum. Methods* 120: 221 (1974)
3. Radeka, V., Rescia, S., *Nucl. Instrum. Methods* A265: 228 (1988)
4. Gillespie, A. B., *Signal, Noise and Resolution in Nuclear Counter Amplifiers*. London: Pergamon (1953)
5. Baldinger, E., Franzen, W., *Adv. Electron. Electron Phys.* 8: 225 (1956)
6. Arecchi, F. T., et al., *Energ. Nucl.* 7: 691 (1960)
7. Radeka, V., Karlovac, N., *Nucl. Instrum. Methods* 52: 86 (1967)
8. Radeka, V., *IEEE Trans. Nucl. Sci.* NS-11: 358 (1964)
9. Bussolati, C., Cova, S., Gatti, E., *Z. Angew. Math. Phys.* 22: 14 (1971)
10. Kandiah, K., Smith, A. J., White, G., In *Proc. 2nd ISPRA Nucl. Electronics Symp.*, Publ. EUR 5370 e: 153. Luxembourg: Euroatom (1975)
11. Nicholson, P. W., *Nuclear Electronics*. New York: Wiley (1974)
12. Bertolaccini, M., et al., *Nucl. Instrum. Methods* 62: 221 (1968)
13. Deighton, M. O., *Nucl. Instrum. Methods* 58: 201 (1968)
14. Konrad, M., *IEEE Trans. Nucl. Sci.* NS-15: 268 (1968)
15. Radeka, V., *IEEE Trans. Nucl. Sci.* NS-15: 455 (1968)
16. Radeka, V., *Nucl. Instrum. Methods* 99: 535 (1972)
17. Goulding, F. S., *Nucl. Instrum. Methods* 100: 493 (1972)
18. Hrisoho, A., *Nucl. Instrum. Methods* 185: 207 (1981)
19. Goulding, F. S., *Nucl. Instrum. Methods* 142: 213 (1977)
20. Goulding, F. S., Landis, D. A., *IEEE Trans. Nucl. Sci.* NS-29: 1125 (1982)
21. Landis, D. A., et al., *IEEE Trans. Nucl. Sci.* NS-29: 619 (1982)
22. Goulding, F. S., Landis, D. A., Madden, N. W., *IEEE Trans. Nucl. Sci.* NS-30: 301 (1983)
23. Pehl, R. H., et al., *IEEE Trans. Nucl. Sci.* NS-32: 22 (1985)
24. Radeka, V., *IEEE Trans. Nucl. Sci.* NS-21: 51 (1974)
25. Radeka, V., Rehak, P., *IEEE Trans. Nucl. Sci.* NS-26: 73 (1979)
26. Radeka, V., Boie, R. A., *Nucl. Instrum. Methods* 178: 543 (1980)
27. Gatti, E., et al., *Nucl. Instrum. Methods* 188: 327 (1981)
28. Macdonald, J. A., ed., *The Time Projection Chamber, AIP Conf. Proc.* No. 108 (1984)
29. Jared, R. C., Landis, D. A., Goulding, F. S., *IEEE Trans. Nucl. Sci.* NS-29: 57 (1982)
30. Gatti, E., et al., *IEEE Trans. Nucl. Sci.* NS-26: 2910 (1979)
31. Boie, R. A., et al., *Nucl. Instrum. Methods* 201: 93 (1982)
32. Boie, R. A., et al., *Nucl. Instrum. Methods* 200: 533 (1982)
33. Smith, G. C., Fischer, J., Radeka, V., *IEEE Trans. Nucl. Sci.* NS-32: 521 (1985)
34. Fischer, J., Radeka, V., Smith, G. C., *Nucl. Instrum. Methods* A252: 239 (1986)
35. Bucholz, D., et al., *Nucl. Instrum. Methods* A253: 481 (1985)
36. Gatti, E., Rehak, P., Walton, J. T., *Nucl. Instrum. Methods* A226: 129 (1984); Rehak, P., et al., *Nucl. Instrum. Methods* A248: 367 (1986)
37. Gatti, E., Manfredi, P. F., *Riv. Nuovo Cimento* Vol. 9, No. 1 (1986)
38. Radeka, V., *Nucl. Instrum. Methods* A226: 209 (1984)
39. Gatti, E., Manfredi, P. F., *Nucl. Instrum. Methods* 226: 142 (1984)
40. Walker, J. T., et al., *Nucl. Instrum. Methods* A226: 200 (1984)
41. Buttler, W., et al., *Nucl. Instrum. Methods* A253: 439 (1987)
42. Vogt, H., *Nucl. Instrum. Methods* A253: 434 (1987)
43. Kleinfelder, S. A., et al., *IEEE Trans. Nucl. Sci.* NS35: 171 (1988)
44. Zimmer, G., *Nucl. Instrum. Methods* 226: 175 (1984)
45. Radeka, V., et al., *IEEE Trans. Nucl. Sci.* NS35: 155 (1988)
46. Ramo, S., *Proc. IRE* 27: 584 (1939)
47. Walenta, A. H., *Nucl. Instrum. Methods* 151: 461 (1978)
48. Rehak, P., In *Proc. Int. Sch. Phys. "Enrico Fermi,"* ed. G. Bologna, M. L. Vincelli. Amsterdam: North-Holland (1983), pp. 25–89
49. Gatti, E., Padovini, G., Radeka, V., *Nucl. Instrum. Methods* 193: 651 (1982)
50. Durand, E., *Electrostatique*, 2: 196. Paris: Masson (1966)
51. Sauli, F., In *Experimental Techniques in High Energy Physics*, ed. T. Ferbel. Menlo Park, CA: Addison-Wesley (1987), p. 79
52. Gordon, J. S., Mathieson, E., *Nucl. Instrum. Methods* 227: 267 (1984)
53. Mathieson, E., Gordon, J. S., *Nucl. Instrum. Methods* 227: 277 (1984)
54. Thompson, J. R., Gordon, J. S., Mathieson, E., *Nucl. Instrum. Methods* A234: 505 (1985)

55. Campbell, N. R., *Proc. Cambridge Philos. Soc.* 15: 117 (1909)
56. Nyquist, H., *Phys. Rev.* 32: 110 (1928)
57. Johnson, J. B., *Phys. Rev.* 32: 97 (1928)
58. Radeka, V., *IEEE Trans. Nucl. Sci.* NS-16: 17 (1969)
59. Sze, S. M., *Physics of Semiconductor Devices*. New York: Wiley (1981)
60. Sansen, W., *Nucl. Instrum. Methods* A253: 427 (1987)
61. Johnson, E. O., *RCA Rev.* 34: 85 (1973)
62. van der Ziel, A., *Proc. IRE* 50: 1808 (1962); 51: 461 (1963)
63. Radeka, V., *IEEE Trans. Nucl. Sci.* NS-20: 182 (1973)
64. Radeka, V., In *Proc. Int. Symp. Nuclear Electronics, Versailles 1968*. Paris: La Documentation Francaise (1968), 1: 1
65. Radeka, V., Chase, R. L., *IEEE Trans. Nucl. Sci.* NS-13: 477 (1966)
66. Mather, J. C., *Appl. Optics* 23: 584 (1984); Moseley, S. H., Mather, J. C., McCammon, D., *J. Appl. Phys.* 56: 1257 (1984)
67. Hrisoho, A., Truong, K., *IEEE Trans. Nucl. Sci.* NS-27: 329 (1980)
68. Fischer, J., et al., *Nucl. Instrum. Methods* A238: 249 (1985)
69. Williams, H. H., *IEEE Trans. Nucl. Sci.* 35: 146 (1988)
70. Tsividis, Y. P., *IEEE J. Solid State Circuits* SC-22: 317 (1987)
71. Richer, J. P., Chase, R. L., *IEEE Trans. Nucl. Sci.* NS-31: 258 (1984)
72. Gatti, E., Radeka, V., *IEEE Trans. Nucl. Sci.* NS-25: 676 (1978)
73. Williams, H. H., *Ann. Rev. Nucl. Part. Sci.* 36: 361 (1986)

Annual Review of Nuclear and Particle Science
Volume 38, 1988

CONTENTS

(*continued*)